***Proc. IMechE- Part N: Journal of Nanomaterials, Nanoengineering and Nanosystems.***

***Accepted February 27th 2019***

***ISSN: 2397-7914; Online ISSN: 2397-7922. Publisher- Sage***

# MODELLING MAGNETIC NANO-POLYMER FLOW WITH INDUCTION AND NANO-PARTICLE SOLID VOLUME FRACTION EFFECTS: SOLAR MAGNETIC NANO-POLYMER FABRICATION SIMULATION

**O. Anwar Bég[1], S. Kuharat[1], M. Ferdows[2], M. Das [3], A. Kadir[1]** and **MD. Shamshuddin[4*]**

*[1]Department of Mechanical/Aeronautical Engineering, Salford University, Manchester, M54WT, **UK**.*
*[2] College of Engineering and Science, Louisiana Tech University, Ruston, 71270, **USA**.*
*[3]Department of Applied Mathematics, University of Dhaka, Dhaka-1000, **Bangladesh.***
*[4]Department of Mathematics, Vaagdevi College of Engineering, Warangal, Telangana, **India**.*

****Corresponding author- email:*** *shammaths@gmail.com*

## ABSTRACT

A mathematical model is presented for the nonlinear steady, forced convection, hydromagnetic flow of electro-conductive magnetic nano-polymer with magnetic induction effects included. The transformed two-parameter, non-dimensional governing partial differential equations for mass, momentum, magnetic induction and heat conservation are solved with the local non-similarity method (LNM) subject to appropriate boundary conditions. Keller's implicit finite difference "box" method (KBM) is used to validate solutions. Computations for four different nanoparticles and three different base fluids are included. Silver nanoparticles in combination with various base fluids enhance temperatures and induced magnetic field and accelerate the flow. An elevation in magnetic body force number decelerates the flow whereas an increase in magnetic Prandtl number elevates the magnetic induction. Furthermore, increasing nanoparticle solid volume fraction is found to substantially boost temperatures. Applications of the study arise in advanced magnetic solar nano-materials (fluids) processing technologies.

**Keywords** *Magneto-nanofluid dynamics; magnetic Prandtl number; magnetic induction; local non-similarity method (**LNM**); Keller box method (**KBM**); magneto-solar nano-materials processing.*

## 1. INTRODUCTION

Magnetic nanofluids have emerged as a new sub-group of nanofluids in energy (and also biomedical engineering) which exhibit both magnetic and thermal enhancement properties. Interest in solar thermo-magnetic nanofluid devices has also grown significantly in the past decade. Some extremely diverse applications of this technology include solar magneto-nanofluid-heat pipes (**MNHP**s) [1], sedimentation control of Arc-Submerged Nanoparticle

Synthesis Systems (**ASNSS**s) with magnetic fields [2], critical heat flux elevation with magnetic nanofluids in phase change processes [3], droplet vaporization time modification in novel rocket combustion systems via magnetized nanofluids [4], thermal tribology [5] and *solar collector magnetic nano-polymer working fluids* [6,7]. In parallel with substantial experimental work, a rich literature has also developed focused on theoretical and computational simulations of magneto-nanofluid dynamic processes. Rarani *et al.* [8] used CFD simulations to evaluate the effect of electromagnetic fields on viscous properties of iron oxide-ethylene glycol magnetized nanofluids. Kandasamy *et al.* [9] employed Lie group transformations and **MAPLE** software to study magnetic nanofluid convection from an extending sheet with wall transpiration. Hamad [10] used hypergeometric functions to analyze magnetic field effects on free convection boundary layer flow from a nanofluid stretching surface. Rana *et al*. [11] used a variational finite element code to model the transient magneto-convective nanofluid dynamics from a rotating extending surface. They employed a Buongiorno model for the nanofluid and showed that primary velocity is strongly retarded with increasing Hartmann number (magnetic parameter) and there is also a reduction in secondary velocity magnitude. Furthermore, temperature and nanoparticle concentrations were found to be accentuated with Hartmann number. Further studies of magnetic nanofluid convective transport have examined mixed convection [12], non-isothermal wall conditions [13], partially heated micro-channels [14], porous media [15] and thermal radiative heat transfer [16].

In numerous modern industrial MHD systems, induction phenomena also arise. These systems include MHD induction furnaces [17], magnetohydrodynamic braking [18] and levitation processing [19]. In such systems mathematical models must also include separate equations for induced magnetic fields, since magnetic Reynolds numbers are of sufficient magnitude in these applications. The induced magnetic field distorts the flow field in MHD induction phenomena. Chen [20] studied uni-directional radiative flux effects on magnetic induction flows with heat transfer. Kumari *et al.* [21] employed a finite difference procedure to study magnetic Prandtl number effects on viscoelastic mixed convection stagnation flow. Zueco and Bég [22] employed an electro-thermal network solver code (**PSPICE**) to simulate Batchelor number effects on magnetohydrodynamic Newtonian squeeze films in a dual-disk braking system for spacecraft. They showed that magnetic Reynolds number is a key parameter dictating the diffusion of magnetic field along streamlines and that Batchelor number successfully predicts the relative ease of slip of the fluid through the magnetic field.

They further determined the correct response of azimuthal and radial induced magnetic field distributions under complex boundary conditions. Further studies of MHD induction phenomena with thermal convection have been communicated by Bég *et al.* [23] for steady flow of liquid metals, "Ahmed *et al.* [24] for unsteady plasma flows and Mahmood *et al.* [25] for transpiring wedge boundary layer flows. Rotational MHD induction flows have also been studied by Haque *et al*. [26], Ghosh *et al.* [27], Bég *et al.* [28] and very recently with entropy generation by Rashidi *et al.* [29]. These investigations have not however considered magnetic nanofluids.

In the present investigation we study the influence of magnetic Prandtl number, nanoparticle solid volume fraction and Prandtl number on magneto-convective nanofluid boundary layer flow with induction effects. A range of different nanofluids is considered and the motivation is to further elucidate the effectiveness of controlling magnetic and thermofluid characteristics with external magnetic fields. This study is also motivated by the potential for magnetized nanofluid microbial fuel cells [30,31]. Recently several researchers have assessed the relative performance of various nanoparticles on convection. Steady Marangoni boundary layer flow with three different types of nanoparticles (copper, aluminum oxide and titanium oxide) has been considered by Remeli *et al.* [32]. Steady two-dimensional Falkner–Skan boundary layer flow with similar solutions for four different types of nanoparticles, (Cu), ($Al_2O_3$), ($TiO_2$) and (Ag) together with two different types of the base fluid, water and ethylene glycol was also analyzed by Khan *et al.* [33]. The present study extends the conventional thermomagnetic nanofluid model [9,10] to the non-similar problem, with different nanoparticles, different base fluids and MHD induction effects. "The induced magnetic field is assumed to be applied parallel to the wall at the outer edge of the boundary layer. The transformed ordinary differential equations are solved numerically with the Sparrow-Yu local non-similarity method (**LNM**) [34]. An error analysis is also performed. Validation of solutions is attained via the Keller box implicit finite difference method (**KBM**). The study is important in simulating transport phenomena in novel nano-magnetic materials processing systems.

## 2. PROBLEM DESCRIPTION

The regime to be studied is depicted in **Fig 1**. Steady, two-dimensional, laminar boundary layer flow of an electrically-conducting, incompressible nanofluid along a plate is

investigated. Magnetic field is applied parallel to the plate i.e. it is aligned with the *x*-coordinate. A constant free stream velocity, $U_\infty$ is present. The streamwise direction is orientated along the *x*-coordinate and the spanwise direction is normal to this i.e. along the *y*-coordinate. "The magnetic field is aligned with the sheet and comprises two mutually perpendicular components, $H\left(H_1, H_2\right)$. Constant thermophysical properties of the nanofluid are assumed. The nanofluid is generalized in the sense that different types of nanoparticles (*Ag, Cu, $Al_20_3$ and $TiO_2$*) are possible as are different base fluids (water etc). The base fluid (i.e. water) and the nanoparticles are in thermal equilibrium and no interphase slip is present. Electrical field, Alfven wave, viscous dissipation and Ohmic heating effects are neglected. Magnetic Reynolds number is sufficiently large however to invoke magnetic induction and this parameter is a quantification of the effect of the flow on the magnetic field distortion. For cases where this parameter is very small (compared to unity) the magnetic field is known to be *undistorted* by the flow. However, for large values of magnetic Reynolds number induction effects are significant and necessitate a separate conservation equation. The normal component of the induced magnetic field, $H_2$ vanishes at the wall and the parallel component, $H_1$ approaches the given value, $H_0$, at the edge of the boundary layer. Wall temperature $T_w$ and the free stream temperature $T_\infty$ are prescribed as constant i.e. the wall is isothermal. The subscripts $\infty$ and *w* denote conditions at the edge of the boundary layer and on the plate surface (wall) respectively. Under the above assumptions, the governing continuity, momentum, magnetic induction and heat conservation equations for MHD nanofluid boundary layer forced convection can be written using Maxwell's generalized electromagnetic field equations, the Navier-Stokes viscous fluid conservation equations and Fourier's heat conduction equation, combining the models of Ferdows *et al.* [16] and Takhar *et al.* [17], as follows:

$$\frac{\partial u}{\partial x}+\frac{\partial v}{\partial y}=0, \tag{1}$$

$$\frac{\partial H_1}{\partial x}+\frac{\partial H_2}{\partial y}=0 \quad , \tag{2}$$

$$u\frac{\partial u}{\partial x}+v\frac{\partial u}{\partial y}=\frac{\mu_{nf}}{\rho_{nf}}\frac{\partial^2 u}{\partial y^2}+\frac{\mu_O}{\rho_{nf}}[H_1\frac{\partial H_1}{\partial x}+H_2\frac{\partial H_1}{\partial y}] \quad , \tag{3}$$

$$u\frac{\partial H_1}{\partial x}+v\frac{\partial H_1}{\partial y}-H_1\frac{\partial u}{\partial x}-H_2\frac{\partial u}{\partial y}=\alpha_1\frac{\partial^2 H_1}{\partial y^2} \quad , \tag{4}$$

$$u\frac{\partial T}{\partial x}+v\frac{\partial T}{\partial y}=\alpha_{nf}\frac{\partial^2 T}{\partial y^2}\ . \tag{5}$$

Velocity, magnetic induction and temperature boundary conditions are prescribed at the wall and in the free stream are as follows:

$$At\ y=0:\ \ u=0, v=0, H_2=\frac{\partial H_1}{\partial y}=0;\ T=T_w\,. \tag{6}$$

$$As\ y\to\infty:\ \ u\to U_\infty, H_1\to H_0, T\to T_\infty\ . \tag{7}$$

To simulate the modified properties of the nanofluid, we define, following Tiwari and Das [35], the effective density of the conducting nanofluid, $\rho_{nf}$, and the effective viscosity of the conducting nanofluid, $\mu_{nf}$, respectively as:

$$\rho_{nf}=(1-\varphi)\rho_f+\varphi\rho_s,\qquad \mu_{nf}=\frac{\mu_f}{(1-\varphi)^{2.5}}\,. \tag{8}$$

Nanofluid heat capacity is given by:

$$(\rho C_p)_{nf}=(1-\varphi)(\rho C_p)_f+\varphi(\rho C_p)_s\,. \tag{9}$$

Thermal conductivity ratio of the *nanofluid* to the *base fluid*, is expressed using the following relation:

$$\frac{k_{nf}}{k_f}=\frac{k_s+2k_f-2\varphi(k_f-k_s)}{k_s+2k_f+2\varphi(k-k_s)}\,. \tag{10}$$

Here $\varphi$ is the solid volume fraction of the nanofluid, $\rho_f$ is the reference density of the (base) fluid fraction, $\rho_s$ is the reference density of the solid fraction, $k_{nf}$ is the thermal conductivity of the nanofluid, $\mu_f$ is the viscosity of the fluid fraction, $k_f$ is the thermal conductivity of the fluid, $k_s$ is the thermal conductivity of the solid. We employ the following transformations to non-dimensionalize eqns. and boundary conditions (1)- (7):

$$\psi(x,y)=(U_\infty\nu_f x)^{\frac{1}{2}}f(\xi,\eta),\ \ \eta(x,y)=\frac{y}{L}\left(\frac{\mathrm{Re}}{\xi}\right)^{\frac{1}{2}},\varphi(\eta,\xi)=H_o\left(\frac{\nu_f x}{U_\infty}\right)^{\frac{1}{2}}g(\xi,\eta),$$
$$\xi(x)=\frac{x}{L},\mathrm{Re}_x=\frac{U_\infty x}{\nu_f},\theta=\frac{T-T_\infty}{T_w-T_\infty}\qquad . \tag{11}$$

Here $\eta$ is the non-dimensional similarity variable, $\xi$ is the non-dimensional transformed stream wise coordinate, $f$ and $g$ are non-dimensional stream and magnetic stream functions, respectively, $\theta$ is non-dimensional temperature function and $Re_x$ is local Reynolds number.

For the *velocity field* we define the dimensional stream function, $\psi(x,y)$ in the usual way employing the familiar Cauchy-Riemann equations:

$$u=\frac{\partial\psi}{\partial y},\quad v=-\frac{\partial\psi}{\partial x}. \tag{12}$$

We utilized the appropriate form of the Cauchy-Riemann equations from electromagnetic field theory for the *induced magnetic field*, magnetic stream function is defined as $\Phi(x,y)$ as follows:

$$H_1=\frac{\partial\Phi}{\partial y},\quad H_2=-\frac{\partial\Phi}{\partial x}. \tag{13}$$

From equation (13) Mass (continuity) and magnetic field continuity are satisfied identically. The boundary value problem defined by eqns. (1)- (7) then reduces to the following trio of coupled, nonlinear *partial* differential equations in a $(\xi,\eta)$ coordinate system, of collectively 8th order.

$$f'\xi\frac{\partial f}{\partial\xi}-\xi ff''\frac{\partial f}{\partial\xi}-\frac{1}{2}ff''-\frac{\frac{1}{(1-\varphi)^{2.5}}}{\left\{(1-\varphi)+\varphi\frac{\rho_s}{\rho_f}\right\}}f'''=\frac{\beta}{\left\{(1-\varphi)+\varphi\frac{\rho_s}{\rho_f}\right\}}\left[g'\xi\frac{\partial g'}{\partial\xi}-\frac{1}{2}gg''-g''\xi\frac{\partial g}{\partial\xi}\right], \tag{14}$$

$$\xi\left(f''\frac{\partial g}{\partial\xi}+f'\frac{\partial g'}{\partial\xi}-g'\frac{\partial f'}{\partial\xi}-g''\frac{\partial f}{\partial\xi}\right)=-\frac{1}{2}gf''+\frac{1}{2}g''f+\lambda g''', \tag{15}$$

$$f'\xi\frac{\partial\theta}{\partial\xi}-\xi\theta'\frac{\partial f}{\partial\xi}-\frac{1}{2}\theta'f=\frac{\frac{1}{\Pr(\frac{k_{nf}}{k_f})}}{\left\{(1-\varphi)+\varphi\frac{(\rho c_p)_s}{(\rho c_p)_f}\right\}}\theta''. \tag{16}$$

where primes denote the differentiation with respect to $\eta$. The transformed boundary conditions assume the form:

$$\eta=0:\ f'(\xi,0)=0;2\xi\frac{\partial f}{\partial\xi}+f=0;g''(\xi,0)=0;g(\xi,0)=0;\theta(\xi,0)=1, \tag{17}$$

$$\eta\to\infty:\ f'(\xi,\eta)=1;\theta(\xi,\eta)=0;g'(\xi,\eta)=1. \tag{18}$$

Here $\Pr=\nu_f\left(\rho C_p\right)_f/k_f$ *is Prandtl number,* $\beta=\mu_0{H_0}^2/{\mu_f}^2$ is magnetic body force number, $\lambda=1/\Pr_m$ i.e. the *reciprocal* of magnetic Prandtl number where $\Pr_m=\nu_f/\alpha_1$ denotes magnetic Prandtl number. In view of the velocity field, the local skin friction coefficient ($Cf_x$) and local Nusselt number (*Nu*) are given by:

$$C_{fx} = \frac{2\tau_w}{\rho U_\infty^2} = \frac{2\mu\left(\frac{\partial u}{\partial y}\right)_w}{\rho U_\infty^2} = 2\,\mathrm{Re}_x^{-0.5}\, f^{//} \Rightarrow C_{fx}[\mathrm{Re}_x]^{\frac{1}{2}} = 2 f^{//}(\xi,\eta)\,, \tag{19}$$

$$Nu = \frac{x\left(\frac{\partial T}{\partial y}\right)_w}{\Delta T} = \mathrm{Re}_x^{0.5}\,\theta'(\xi,\eta)\,. \tag{20}$$

Here $\tau_w$ is the shear stress at the wall, $\left(\partial T/\partial y\right)_w$ is the temperature gradient at the wall, $\Delta T = T_\infty - T_w$ is the temperature difference. In a similar fashion we may define a local magnetic induction gradient. In the simulations four different nanoparticles and three different base fluids are studied. The appropriate properties are summarized in **Table 1**: The two-point BVP define by eqns. (14)- (16) under conditions (17), (18) is well-posed. It generally requires a numerical solution for which many techniques are possible including finite elements, spectral methods and network simulation. The adoption of the Tiwari-Das model [35] avoids the generation of a third boundary layer equation for species conservation. This approach has recently also been implemented for a number of multi-physical nanofluid transport problems. Rashidi *et al.* [36] used Homotopy algorithms to simulate nanofluid convection from a cylindrical body with the Tiwari-Das model. Anwar Bég *et al.* [37] studied nanofluid migration in re-charging geothermal systems using a finite difference algorithm and both the Tiwari-Das model and other nanoscale transport models. Anwar Bég and Tripathi [38] presented the first rigorous study of peristaltic flow of Tiwari-Das nanofluids in actuated medical pump systems. Rana *et al.* [39] used a variational finite element code to study the influence of body inclination on Tiwari-Das nanofluid convection from a tilted cylinder. These studies have confirmed the robustness of the Tiwari-Das model and verified that it accurately characterizes actual nanofluids in engineering systems without the necessity for an additional species conservation equation for nano-particles.

## 3. SPARROW-YU LOCAL NON-SIMILARITY METHOD (LNM) NUMERICAL SOLUTIONS

In the present study we implement a well-established computational procedure known as local non-similarity method (LNM) which was developed by Sparrow and Yu [34]. This method has been adapted to solve an extensive range of boundary layer flow problems and is lucidly described in Kao [40]. More recently LNM has been used to analyze chemo-magnetic heat transfer [41], radiative rheological cross-diffusion flows in porous media [42], convection with viscous heating effects [43], axisymmetric transient boundary layers [44],

heat transfer from titled solar collectors [45] and magnetic induction flows [46]. Anwar Bég [47] has recently reviewed the relative efficiency and versatility of **LNM** compared with other computational approaches including spectral methods and alternating finite difference algorithms. **LNM** embodies two essential features. First the *non-similar* solution at any *specific streamwise location* is found (i.e. each solution is locally autonomous). Second, the local solutions are found from the appropriate differential equations. These equations can be solved numerically by well-established techniques, such as forward integration (e.g. a Runge-Kutta quadrature) in conjunction with a shooting procedure to determine the unknown boundary conditions at the wall. The method also allows some degree of self-checking for accuracy of the numerical results. It is easily interfaced with modern symbolic programs such as **MATHEMATICA, MATLAB** and **MAPLE**. In approaching the local non-similarity solution of eqns. (14) to (16), it is first convenient to eliminate the explicit presence of the $\xi$-derivatives of the dimensionless stream function, $f$, and dimensionless temperature function, $\theta$, by defining:

$$G_1 = \frac{\partial f}{\partial \xi}, G_1^{/} = \frac{\partial f^{/}}{\partial \xi}, G_1^{//} = \frac{\partial f^{//}}{\partial \xi}, G_1^{///} = \frac{\partial f^{///}}{\partial \xi}, \tag{21}$$

$$G_2 = \frac{\partial g}{\partial \xi}, G_2^{/} = \frac{\partial g^{/}}{\partial \xi}, G_2^{//} = \frac{\partial g^{//}}{\partial \xi}, G_2^{///} = \frac{\partial g^{///}}{\partial \xi}, \tag{22}$$

$$G_3 = \frac{\partial \theta}{\partial \xi}, G_3^{/} = \frac{\partial \theta^{/}}{\partial \xi}, G_3^{//} = \frac{\partial \theta^{//}}{\partial \xi}. \tag{23}$$

$G_1, G_2, G_3$ represent three additional unknown functions. Therefore, it is necessary to deduce three further equations to determine the $G_1, G_2, G_3$ .This is accomplished by creating *subsidiary equations* by differentiation of the transformed conservation equations and boundary conditions (i,e. the $G_1, G_2, G_3$ system of equations) with respect to $\xi$. The subsidiary equations for $G_1, G_2, G_3$ contain terms, $\partial G_1 / \partial \xi, \partial G_2 / \partial \xi, \partial G_3 / \partial \xi$ and their $\eta$ -derivatives. When these terms are ignored the system of equations for $f$, $g$, $\theta$, $G_1$, $G_2$, $G_3$ reduces to a system of *ordinary* differential equations that provide locally autonomous solutions. This form of the local non-similarity method is referred to as the *second level of truncation*, since approximations are made by dropping terms in the second level equation. After the substitution of these quantities and then differentiated with respect to $\xi$, giving (with boundary conditions):

$$AG_1^{///} + \frac{1}{2} fG_1^{//} + \frac{3}{2} f^{//} G_1 + \xi G_1 G_1^{//} - f^{/} G_1^{/} - \xi (G_1^{/})^2 = K\left[\frac{1}{2} gG_2^{//} + \frac{3}{2} g^{//} G_2 + \xi G_2 G_2^{//} - g^{/} G_2^{/} - \xi (G_2^{/})^2\right], \tag{24}$$

$$\xi G_2 G_1^{//} + \frac{3}{2} f^{//} G_2 + f^{/} G_2^{/} - g^{/} G_1^{/} - \frac{3}{2} g^{//} G_1 - \xi G_1 G_2^{//} = -\frac{1}{2} g G_1^{//} + \frac{1}{2} f G_2^{//} + \lambda G_2^{///}, \quad (25)$$

$$f^{/} G_3 + \xi G_3 G_1^{/} - \xi G_1 G_3^{/} - \frac{3}{2} \theta^{/} G_1 - \frac{1}{2} f G_3^{/} = \frac{1}{\mathrm{Pr}_{nf}} G_3^{//} \cdot \quad (26)$$

$$\eta = 0: \; G_1^{/}(\xi,0) = 0; \; G_1(\xi,0) = 0; \; G_2^{//}(\xi,0) = 0; \; G_2(\xi,0) = 0; \; G_3(\xi,0) = 0, \quad (27)$$

$$\eta \to \infty: G_1^{/}(\xi, L) = 0; G_2(\xi, L) = 0; G_2^{/}(\xi, L) \; as \; L \to \infty. \quad (28)$$

$\xi$ -derivative terms which are explicitly involving are grouped on the righthand sides. Equations (24)-(25) are essentially *auxiliaries* to the conservation equations and their boundary conditions. The functions $f$, $G_1$ appear in these equations. By the same token, the functions $g, G_2, \theta, G_3$ are present in these equations, necessitating simultaneous solution. The *non-similarity* solution method preserves the two attractive features of the local-similarity method, that is, for any given $\xi$, the solution is independent of that at any other $\xi$ and we can solve the resulting equations as if they were *ordinary* differential equations of the similarity-type. Furthermore, the local non-similarity approach retains all terms in the momentum, magnetic induction and energy equations, as is evidenced in equations (24)- (26). From subsidiary equations that is, from the $G_1, G_2, G_3$ equations, the terms are deleted. This is in contrast to the local-similarity method, where terms are deleted from the momentum and energy equations themselves. We consider the new functions:

$$h_1 = f^{//}, h_2 = g^{/}, h_3 = \theta^{/}, \quad (29)$$

$$h_4 = \frac{\partial f^{//}}{\partial \xi}, h_5 = \frac{\partial g^{/}}{\partial \xi}, h_6 = \frac{\partial \theta^{/}}{\partial \xi}. \quad (30)$$

Now the nonlinear differential equations (14)- (16) and (24)- (26) with the boundary conditions (17), (18) and (27), (28) "have been solved numerically, employing the sixth order implicit Runge-Kutta-Butcher (**RKB**) initial value problem solver along with Nachtsheim-Swigert iteration technique, in **MAPLE**. In the shooting method technique $h_1, h_2, h_3, h_4, h_5, h_6$ are considered as missing conditions at the initial point and the differential equations are then integrated numerically from the initial value to the terminal point. Thereafter the user checks the accuracy of the guess for the missing initial condition with the *calculated value* of the dependent variable at the end point with its given value there. Then one considers another value of the missing initial condition and the process is repeated and continued until the agreement between the calculated and the given condition at the terminal point is within the specified degree of accuracy. Here we have also computed the error of the initial guess values

($h_1, h_2, h_3, h_4, h_5, h_6$). We consider 0.0001 as initial guess values. The following equation is used to evaluate the percentage error (PE):

$$PE = \frac{|h^* - hi|}{h^*} \times 100\% \ . \tag{31}$$

Where $PE$= percentage of error of guess values, $h^*$ = initial guess values (0.0001) and $h_i$ denote the calculated values ($i$ = 1….6). **Table 2** documents the errors computed with **LNM**.

## 4. VALIDATION WITH KELLER BOX FINITE DIFFERENCE METHOD (KBM)

In order to validate the present **RKB** shooting computations, the Keller-Box implicit difference method is also utilized to solve the nonlinear boundary value problem defined by eqns. (14)- (16) with the boundary conditions (17), (18). This second order accurate method is ideal for *parabolic* problems i.e. boundary layer flows. Recently the **KBM** algorithm has successfully resolved a number of nonlinear magnetohydrodynamics and nanofluid dynamics problems including micropolar nanofluid enrobing flows [48], Hall MHD generator transport [49], viscoelastic flows in porous media [50] and biological micro-organism propulsion [51]. The Keller-Box discretization is fully coupled at each step which reflects the physics of parabolic systems – which are also fully coupled. Discrete calculus associated with the Keller-Box scheme has also been shown to be fundamentally different from all other mimetic (physics capturing) numerical methods, as elaborated by Keller [52]. The Keller Box Scheme comprises four stages:

1)Decomposition of the $N^{th}$ order partial differential equation system to $N$ first order equations.

2)Finite Difference Discretization.

3)Quasi-linearization of Non-Linear Keller Algebraic Equations.

4)Block-tridiagonal Elimination solution of the Linearized Keller Algebraic Equations.

A two-dimensional computational grid is imposed on the $\xi$-$\eta$ plane. The stepping process is defined by:

$$\eta_0 = 0, \quad \eta_i = \eta_{i-1} + h_j, \quad j = 1, 2, ..., \mathrm{J}, \quad \eta_J \equiv \eta_\infty, \tag{32}$$

$$\xi^0 = 0, \quad \xi^n = \xi^{n-1} + k_n, \quad n = 1, 2, ..., N \, . \tag{33}$$

where $k_n$ is the $\Delta\xi$ - spacing and $h_j$ is the $\Delta\eta$ - spacing. If $g_j^n$ denotes the value of *any general variable* at $\left(\eta_j, \xi^n\right)$, then the variables and derivatives of Equations (14)-(16) at $\left(\eta_{j-1/2}, \xi^{n-1/2}\right)$ are replaced by:

$$g_{j-1/2}^{n-1/2} = \frac{1}{4}\left(g_j^n + g_{j-1}^n + g_j^{n-1} + g_{j-1}^{n-1}\right), \tag{34}$$

$$\left(\frac{\partial g}{\partial \eta}\right)_{j-1/2}^{n-1/2} = \frac{1}{2h_j}\left(g_j^n - g_{j-1}^n + g_j^{n-1} - g_{j-1}^{n-1}\right), \tag{35}$$

$$\left(\frac{\partial g}{\partial \xi}\right)_{j-1/2}^{n-1/2} = \frac{1}{2k^n}\left(g_j^n - g_{j-1}^n + g_j^{n-1} - g_{j-1}^{n-1}\right). \tag{36}$$

The resulting finite-difference approximation of equations (14)-(16) for the mid-point $\left(\eta_{j-1/2}, \xi^n\right)$, are then generated. This non-linear system of algebraic equations is linearized by means of Newton's method, as described by Anwar Bég *et al.* [50]. The linearized system is solved by the block-elimination method, since it possesses a block-tridiagonal structure. The bock-tridiagonal structure generated consists of *block matrices*. The complete linearized system is formulated as a *block matrix system*, where each element in the coefficient matrix is a matrix itself, and this system is solved using the efficient Keller-box method. The numerical results are strongly influenced by the number of mesh points in both directions. After some trials in the $\eta$-direction (radial coordinate) a larger number of mesh points are selected whereas in the $\xi$-direction (tangential coordinate) significantly less mesh points are utilized. $\eta_{\max}$ has been set at 12 and this defines an adequately large value at which the prescribed boundary conditions are satisfied. $\xi_{\max}$ is set at 3.0 for this flow domain. Mesh independence is achieved in the present computations. The numerical algorithm is executed in **MATLAB** on an Octane SGI workstation and computes in seconds. The method demonstrates excellent stability, convergence and consistency, as elaborated by Keller [52]. Comparison computations for performance of different nanofluids with aluminum oxide-water nanofluid ($Al_2O_2$-$H_2O$) in terms of percentage (increase (+) or decrease (-)) via both **LNM** and **KBM** approaches is documented in **Tables 3a** and **3b**. **Tables 3a, b** and **4** indicate that generally *silver water and silver oxide water nanofluids* yield the best performance relative to the benchmark nanofluid considered i.e. aluminum oxide-water nanofluid. Excellent correlation is achieved as observed in **Tables 3a, b**. Confidence in the present LNM solutions is therefore high. Further computations with **LNM** are given in **Table 4**.

## 5. LNM COMPUTATIONS, CONVERGENCE, RESULTS AND DISCUSSION

The two-point non-linear partial differential **BVP** has been solved numerically using the local non-similarity method (**LNM**). Here, a brief discussion is presented on the *convergence* of

the solution. In due course we present graphical results for the influence of the emerging thermophysical parameters ( $\xi$, $\lambda$, $\beta$, $\phi$ and $Pr$ ) and nanofluid type on velocity, magnetic stream function gradient and temperature distributions. The values of the step size $\Delta\eta$ in $\eta$ and the infinity condition at the edge of boundary layer ( $\eta \to \infty$ ) have to be adjusted for different values of the parameters to maintain accuracy. Throughout this study, we prescribe the value of $\Delta\eta = 0.05$ and was found to be satisfactory for a convergence criterion of $10^{-5}$ which gives four decimal places accuracy. The edge of the boundary layer is selected, between 5 and 10. We have plotted skin friction coefficient $f''(\xi,0)$, local Nusselt number (*Nu*) and the induced magnetic stream function gradient profiles $g'(\xi,0)$, by using a step size $\Delta\xi = 0.5$. The value of $\xi_\infty$ (i.e. the edge of the boundary layer) is taken as 3.0. A convergence criterion based on the relative difference between the current and previous iteration values is employed. When the difference reaches less than $10^{-5}$ the solution is assumed to have converged and the iterative process is terminated. The numerical code is executed in **MATLAB**. Dimensionless temperature $\theta(\xi,\eta)$, and temperature gradients $\theta'(\xi,0)$, are also computed, the latter with respect to non-similar parameter ( $\xi$ ). We have elected to study initially the different performances of the four nano-particles under investigation, viz *copper, silver, silver oxide* and *titanium oxide* in individual combination with the three different base fluids (water, ethylene glycol (*EG*) and kerosene (*Ke*). In order to illustrate the results graphically, the numerical values are plotted in **Figs (1-13) a-c**. In all cases, the **LNM** approach achieves excellent stability and convergence.

**Figs. 2a-2c** illustrate the velocity, magnetic stream function gradient and thermal distributions for different nanofluid suspensions. Here the parameter $\lambda$ (reciprocal of the magnetic Prandtl number) is set at 0.5- this indicates that magnetic Prandtl number is 2 i.e. *viscous diffusion rate* is double the *magnetic diffusion rate* (or magnetic Reynolds number is twice the ordinary Reynolds number). Magnetic induction effects are therefore weak. Evidently in fig. 2a the greatest acceleration is achieved for silver nanofluids (silver nano-particles in different base fluids). Silver kerosene achieves the highest velocities followed by silver-water and then silver ethylene glycol. The lowest velocities however correspond to silver oxide nanofluid (silver oxide kerosene, then silver oxide water and finally silver oxide ethylene glycol). Copper-nanofluid suspensions are observed to achieve better velocities than titanium oxide-nanofluids, “although the latter still perform better than silver oxide

nanofluids. Asymptotically smooth behaviour of all profiles is achieved at the edge of the boundary layer testifying to the satisfactory convergence of solutions. Fig 2b reveals similar performance to the velocity field- the silver-nanofluids again produce the highest magnitudes of magnetic stream function gradient (induced magnetic field function), and titanium oxide and silver oxide yield the lowest. Copper nanofluid outperforms both titanium oxide and silver oxide but again is superseded by the silver nanofluid case, the latter demonstrating again that silver-kerosene is the highest achiever. Conversely in fig. 2c we observe that the best heat transfer enhancement is obtained with titanium oxide-water nanofluid (the other titanium oxide suspensions achieve very good performance also) whereas the poorest performance corresponds to copper-nanofluids, specifically copper-kerosene nano-suspension. Silver and silver oxide nanofluid also yield high temperatures, although they are clearly exceeded with the titanium oxide suspensions.

**Figs 3a-c** shows the velocity, magnetic stream function gradient and thermal distributions for different nanofluid suspensions, for $\lambda = 1$ (all other parameters are unaltered). In this case therefore magnetic Prandtl number is also unity and *viscous diffusion rate* is exactly equal to *magnetic diffusion rate* (magnetic Reynolds number is identical in magnitude to ordinary Reynolds number). Magnetic induction effects are therefore anticipated to be stronger than in figs 2a-c. Indeed, magnitudes of velocities, induced field and temperature are all greater than the corresponding figs 2a-c. Very similar trends are also obtained i.e. silver-nanofluids generate the greatest acceleration, highest magnitudes of magnetic stream function gradient (induced magnetic field function), and titanium oxide-water nanofluid achieves the highest temperatures.

**Figs 4a-c** illustrate the velocity, magnetic stream function gradient and thermal distributions for different nanofluid suspensions. In these plots, however $\lambda = 5$ *and* $\beta = 0.5$ *whereas* $\phi$ *and* Pr *remain the same*. The magnetic Prandtl number $\mathrm{Pr}_m = \nu_f / \alpha_1$ is therefore 0.2, significantly lower than in figs 2a-c or 3a-c and *magnetic diffusion rate* is five times the *viscous diffusion rate* (magnetic Reynolds number is one fifth of ordinary Reynolds number). Furthermore, the magnetic body force number is much higher than in figs 2a-c and 3a-c. $\beta = \mu_0 {H_0}^2 / {\mu_f}^2$ which represents the magnetic drag force to viscous force ratio. Larger values of $\beta$ will therefore imply more significant applied magnetic field in the regime, as elaborated by Ghosh *et al.* [27]. The general trends observed in figs 2a-c, 3a-c are also computed in figs

4a-c. Comparing fig 4a with fig 2a, fig 3a, it is immediately apparent that with greater applied magnetic field ($H_o$), the velocity distributions are all modified from a monotonic increase to a sharper plateau pattern attained at smaller values of transverse coordinate. This indicates that the velocity field is decelerated, and boundary layer thickness is increased with larger $\beta$ values. Comparing figs 4b with figs 2b, 3b, we infer that there is a significant boost in induced magnetic field function and, in particular, a marked enhancement at the plate surface. However, near the boundary layer free stream, magnetic induction values are found to be depleted somewhat with larger magnetic force numbers. Increasing applied magnetic field therefore also enhances induced magnetic field. Comparing fig. 4c and figs 2c, 3c, the temperature fields are not altered significantly. This may be attributable to the absence of Joule heating (Ohmic dissipation) effects in the energy equation, which is the primary mechanism for energy dissipation in magnetohydrodynamic flows and conversion of kinetic energy to heat, as discussed by Kumari and Nath [21].

**Figs. 5a-c** demonstrates the velocity, magnetic stream function gradient and thermal distributions for different nanofluid suspensions. In these plots, $\lambda = 10, \beta = 0.7$ i.e. greater than in figs 4a-c. The magnetic Prandtl number $\mathrm{Pr}_m = \nu_f / \alpha_1$ is now 0.1, significantly lower than in figs 2a-c or 3a-c and *magnetic diffusion rate* is ten times the *viscous diffusion rate* (magnetic Reynolds number is one tenth ordinary Reynolds number). Magnetic body force number, $\beta = \mu_0 H_0^{\,2} / \mu_f^{\,2}$ is also higher, and magnetic force is 70% the viscous force. The trends observed in figs 4a-c are further amplified with the new data. In particular, the magnetic induction is found to be even greater at the wall. Magnetic boundary layer thickness will therefore also be increased.

**Figs 6a-c** shows the velocity, magnetic stream function gradient and thermal distributions for different nanofluid suspensions, with all data identical to figs 3a-c, i.e. $\lambda = 1, \beta = 0.2$, except solid volume fraction, $\phi = 0.1$ (half that in fig 3c) "and $Pr = 3.77$. There is no tangible modification in velocity profiles or induced magnetic field (magnetic stream function gradient) profiles. However, temperatures are found to be slightly elevated in figs 6c compared with fig 3c. Prandtl number defines the ratio of viscous diffusion to thermal diffusion in the boundary layer regime. For $\mathrm{Pr} > 1$, momentum diffusivity will exceed thermal diffusivity, which applies to figs 3c and 6c. Momentum boundary layer thickness will

also exceed thermal boundary layer thickness. Prandtl number = $\nu_f \left(\rho C_p\right)_f / k_f$ also represents the product of dynamic viscosity and specific heat capacity divided by thermal conductivity of the primary fluid. Higher Pr fluids (fig 3c, $\mathrm{Pr} = 4.17$) will therefore possess a much lower thermal conductivity and this will result in lower temperatures in the boundary layer. Conversely lower Pr fluids (fig. 6c, $\mathrm{Pr} = 3.77$) will possess higher thermal conductivity and will generate greater temperatures. The lower solid volume fraction in fig 6c compared with fig 3c will also act to decrease temperatures, but this effect is over-shadowed by the lower Prandtl number.

**Figs 7a-c** depict velocity, magnetic stream function gradient and thermal distributions for different nanofluid suspensions, with all data identical to figs 6a-c, i.e. $\lambda = 1, \beta = 0.2$ ,but increases in solid volume fraction and Prandtl number, $\phi = 0.5$ and $\mathrm{Pr} = 6.2$ .Significant enhancement in temperature in fig 7c compared with fig 6c. Silver oxide water nanofluid achieves the highest temperatures whereas copper-kerosene nanofluid yields the lowest temperatures. Even though the increase in Prandtl number will result in a lowering in temperature, the large increase in solid volume fraction (it is five times greater in fig 7c relative to that in fig 6c) will swamp the Prandtl number effect and manifest in an effective thermal enhancement, leading to a substantial thickening in the thermal boundary layer.

**Figs. 8a-c** illustrates the influence of magnetic body force number ( $\beta$ ) on the distributions of surface shear stress, $f''(\xi, 0)$, magnetic stream function gradient, $g'(\xi, 0)$, with non-similar parameter ( $\xi$ ), for copper-water and copper-ethylene glycol nanofluids. Here we have prescribed $\lambda = 0.5, \phi = 0.5$ and $\mathrm{Pr} = 4.17$. Shear stress (fig. 8a) is observed to be maximized with *copper water nanofluid* and low magnetic force number. The smaller applied magnetic field associated with lower $\beta$ will generate a weaker Lorentzian magnetic drag force, and this will effectively accelerate the flow causing a rise in shear stresses at the wall. Shear stress is clearly minimized with the largest value of $\beta = 0.4$ and copper ethylene glycol nanofluid. Magnetic stream function gradient, $g'(\xi, 0)$, as shown in fig 8b, is also maximized for *copper water nanofluid* and low magnetic force number and minimized with the largest value of $\beta = 0.4$ and copper ethylene glycol nanofluid. Heat transfer rate at the plate is shown in fig 8c to be maximum for the copper-water nanofluid at maximum magnetic force parameter.

The copper ethylene glycol nanofluid with lowest magnetic force number achieves the lowest heat transfer gradient.

**Figs. 9a-c** demonstrates the effect of present the influence of reciprocal of magnetic Prandtl number ($\lambda$) on the distributions of surface shear stress, $f''(\xi,0)$, magnetic stream function gradient, $g'(\xi,0)$ *and* temperature gradient profiles, $\theta'(\xi,0)$ with non-similar parameter ($\xi$), for copper-water and copper-ethylene glycol nanofluids. Here we have prescribed $\beta = 0.5, \phi = 0.1$ and $\Pr = 4.17$. Shear stress is generally maximized with the largest value of prescribed $\lambda(=1.0)$ and for copper-water nanofluid. It is however minimized for copper ethylene glycol nanofluid at intermediate reciprocal of magnetic Prandtl number $(\lambda = 0.7)$. The highest heat transfer gradient corresponds to copper water nanofluid at $\lambda = 0.7$. *Copper ethylene glycol* nanofluid yields the lowest (most negative) values for heat transfer gradient with the minimal value of reciprocal of magnetic Prandtl number ($\lambda = 0.7$).

**Figs. 10a-c** shows the effect of present the influence of magnetic body force number ($\beta$) on the distributions of surface shear stress, $f''(\xi,0)$, magnetic stream function gradient, $g'(\xi,0)$ *and* temperature gradient profiles, $\theta'(\xi,0)$ with non-similar parameter ($\xi$), for silver-water and silver-ethylene glycol nanofluids with $\lambda = 0.5, \phi = 0.5$ and $\Pr = 4.1$. Silver water nanofluid with low $\beta$ is found to maximize shear stress whereas (fig. 10a), whereas silver-ethylene glycol nanofluid with high $\beta$ minimizes shear stress. Clearly the magnetic force parameter acts to decelerate the flow. A similar response is detected for the induced magnetic field gradient in fig 10b. Fig 10c demonstrates that silver water nanofluid with high $\beta(=0.4)$ *is associated with* maximum heat transfer gradient and silver-ethylene glycol nanofluid with low $\beta(=0.2)$ minimizes heat transfer gradient, $-\theta'(\xi,0)$.

**Figs. 11a-c** presents the effect of present the influence of reciprocal of magnetic Prandtl number ($\lambda$) on the distributions of surface shear stress, $f''(\xi,0)$, magnetic stream function gradient, $g'(\xi,0)$ *and* temperature gradient, $\theta'(\xi,0)$ ,with non-similar parameter ($\xi$), for silver-water and also silver-ethylene glycol nanofluids with $\beta = 0.5, \phi = 0.1$ and $\Pr = 4.17$. The highest shear stress is associated with silver-ethylene glycol nanofluids for the case

where $\lambda = 1$(maximum) whereas the lowest shear stress corresponds to silver water nanofluid with intermediate reciprocal of magnetic Prandtl number ($\lambda = 0.7$). Induced magnetic field gradient is conversely found to be maximized with silver water nanofluid with $\lambda$ = 1, whereas it is minimized for the with silver-ethylene glycol nanofluids for $\lambda = 10.5$. Evidently smaller magnetic Prandtl numbers (larger $\lambda$ values), as elaborated earlier act to boost the magnetic induction effect. As with the shear stress distribution (fig 11a), the temperature gradient is largest for silver-ethylene glycol nanofluids with $\lambda = 0.7$ (intermediate) whereas it is a minimum for silver water nanofluid with maximum reciprocal of magnetic Prandtl number ($\lambda = 1$, *for which magnetic Prandtl number is unity*).

**Figs. 12a-c** present the influence of reciprocal of magnetic Prandtl number ($\lambda$) on the distributions of surface shear stress, $f''(\xi,0)$, magnetic stream function gradient, $g'(\xi,0)$ *and* temperature gradient, $\theta'(\xi,0)$ with non-similar parameter ($\xi$), for silver-oxide water and silver oxide-ethylene glycol nanofluids with $\beta = 0.5, \phi = 0.1$ and $\mathrm{Pr} = 4.17$ with various reciprocals of magnetic Prandtl number ($\lambda$). Silver oxide-ethylene glycol nanofluid with $\lambda = 0.5$ attains the maximum shear stress (fig 12a), whereas silver oxide-water nanofluid with $\lambda = 1.0$ yields the lowest shear stress. Boundary layer thickness is therefore least with silver oxide-ethylene glycol and acceleration is highest. Magnetic stream function gradient, $g'(\xi,0)$ is observed to be highest in fig 12b, with silver oxide-ethylene glycol nanofluid with $\lambda = 1.0$ and to be *lowest* for silver oxide-water nanofluid with $\lambda = 0.5$. Temperature gradient is found to be maximized (fig. 12c) with silver oxide-water nanofluid with $\lambda = 1.0$. Silver oxide-ethylene glycol achieves the lowest temperature gradient with $\lambda = 0.5$.

Influence of magnetic body force numbers ($\beta$) on the distributions of surface shear stress, $f''(\xi,0)$, magnetic stream function gradient, $g'(\xi,0)$ *and* temperature gradient, $\theta'(\xi,0)$, with non-similar parameter ($\xi$), for silver-oxide water and silver oxide-ethylene glycol nanofluids with $\lambda = 0.5, \phi = 0.1$ and $\mathrm{Pr} = 4.17$ are illustrated in **Figs. 13a-c**. Silver oxide water nanofluid attains the highest magnitudes of shear stress (fig. 13a), with weakest magnetic body force ($\beta = 0.2$). Silver oxide-ethylene glycol nanofluid corresponds to the minimum shear stress for the strongest magnetic body force ($\beta = 0.4$). Evidently shear stress is depleted with greater applied magnetic field strengths and this will decelerate the flow and lead to a

thicker boundary layer for silver oxide-ethylene glycol. On the contrary, magnetic field stream function gradient is observed to be largest for silver oxide-ethylene glycol (with lowest $\beta$) in fig 13b, whereas silver oxide water nanofluid at highest $\beta$ results in the least magnitudes of $g'(\xi,0)$. Finally, in fig 13c, it is evident that silver oxide-ethylene glycol (with maximum magnetic body force parameter ( $\beta = 0.4$ ) generates the highest heat transfer gradient. Silver oxide water nanofluid with weak magnetic body force corresponds to the lowest magnitudes of heat transfer gradient. These computations concur with Jang and Choi [53]. It is further to be noted that all nanofluid data has been selected based on actual experimental values available in Bianco *et al.* [54] and Das *et al.* [55].

## 6. CONCLUDING REMARKS

In current simulation, we have developed numerical solutions for non-similar steady magnetized nanofluid boundary layer flow with induced magnetic field effects. The transformed partial differential equations for momentum, magnetic induction and energy conservation have been solved subject to physically realizable boundary conditions, with the Sparrow-Yu local non-similarity method (**LNM**) and shooting quadrature. Extensive validation with the Keller box method (KBM), a finite difference second order algorithm. A parametric investigation has been conducted for the influence of solid volume fraction, magnetic force number, reciprocal of the magnetic Prandtl number, ordinary Prandtl number and local non-similarity variable (stream wise coordinate) on velocity, magnetic stream function gradient, temperature profiles, shear stress and temperature gradient distributions. The relative performance of four nanoparticles (copper, silver, silver oxide, titanium oxide) and three different base fluids (water, ethylene glycol and kerosene) have been evaluated. The computations executed with **MAPLE** software, have shown:

- The best overall performance is achieved with silver nanoparticles.
- Thermal enhancement is generally maximized when water is utilized as the base fluid, although in certain cases ethylene glycol also performs very efficiently.
- Increasing the magnetic force number decelerates the boundary layer flow
- Increasing the magnetic Prandtl number generally accentuates magnetic induction.
- Increasing Prandtl number decreases temperatures and reduces thermal boundary layer thickness.

- Increasing nanoparticle solid volume fraction elevates temperatures.

The present study has considered *steady-state* flow near-wall dynamics of manufacturing of solar magnetic nano-polymers. Future investigations will examine actual implementation of these fluids in solar collector configurations with radiative heat transfer (solar flux) and efforts in this regard are currently underway using the ANSYS FLUENT computational fluid dynamics code as elaborated by Kuharat [56]. Furthermore, other possible extensions to the current work may involve the exploration of electrical field effects [57], nano-particle shape effects [58] and non-Newtonian behaviour [59, 60]. These offer further potential applications for electro-magnetic nano-polymers and are currently being considered in solar engineering by the authors.

## REFERENCES


1. Chiang YC, Chieh JJ and Ho CC. (2012) The magnetic-nanofluid heat pipe with superior thermal properties through magnetic enhancement. *Nanoscale Res Lett* 2012; 7(1): 322 (6 pages). https://doi.org/10.1186/16-276X-7-322.
2. Chang H, Tsung TT, Lin CR, Lin HM, Lin CK, Lo CH, Su HT. A study of magnetic field effect on nanofluid stability of CuO. *Materials Transactions* 2004; 45(4):1375-1378.
3. Lee T, Lee JH and Jeong YH. Flow boiling critical heat flux characteristics of magnetic nanofluid at atmospheric pressure and low mass flux conditions. *Int J Heat Mass Transfer* 2013; 56:101-106.
4. Cristaldo CFC, Bakuzis A, De Bortoli AL and Fachini FF. Extended numerical analysis for the magnetic nanofluid droplet heating and vaporization 13th Brazilian Congress of Thermal Sciences and Engineering- Workshop em Engenharia e Tecnologia Espaciais, May 3-5, Rio de Janeiro, Brazil, 2011.
5. Vékás L. Magnetic nanofluids properties and some applications. *Romanian J Phys* 2004; 49(9):707-721.
6. Prabu T and Ajay Sekar C. Improving heat transfer in hybrid solar systems using liquid metal alloys as a coolant. *ASME J Sol Energy Eng* 2017; 139(6): 064501-064501-4.
7. Khalil K and Vafai K. A review on the applications of nanofluids in solar energy field. *Renewable Energy* 2018; 123:398-406.
8. Rarani EM, Etesami N and Esfahany MN. Influence of the uniform electric field on viscosity of magnetic nanofluid ($Fe_3O_4$-EG). *J Appl Phys* 2012 ;112 :094903-1-094903-6.
9. Kandasamy R, Loganathan P and Arasu PPP. Scaling group transformation for MHD boundary-layer flow of a nanofluid past a vertical stretching surface in the presence of suction/injection. *Nuc Eng Des* 2011; 241: 2053-2059.
10. Hamad MAA. Analytical solution of natural convection flow of a nanofluid over a linearly stretching sheet in the presence of magnetic field. *Int Commun Heat Mass Transfer* 2011; 38:487-492.
11. Rana P, Bhargava R and Anwar Bég O. Finite element simulation of unsteady magneto-hydrodynamic transport phenomena on a stretching sheet in a rotating nanofluid. *Proc IMechE- Part N: J Nanoengineering and Nanosystems* 2013; 227(2): 77–100.

12. Ferdows M, Khan MS, Alam MM and Sun S. MHD mixed convective boundary layer flow of a nanofluid through a porous medium due to an exponentially stretching sheet. *Math Prob Eng* 2012; Article ID 408528:1-21.
13. Hamad MAA, Pop I and Ismail AIM. Magnetic field effects on free convection flow of a nanofluid past a vertical semi-infinite flat plate. *Nonlinear Analysis: Real World Applications* 2011; 12:1338-1346.
14. Aminossadati SM, Raisi A and Ghasemi B. Effects of magnetic field on nanofluid forced convection in a partially heated microchannel. *Int J Nonlinear Mech* 2011; 46:1373-1382.
15. Eldabe NTM, lbashbeshy MAE and Elsai EM. Effect of magnetic field on flow and heat transfer over an unsteady stretching surface embedded in a porous medium filled with nanofluid. *Int J Energy Tech* 2013; 5(6):1-8.
16. Ferdows M, Khan MS and Anwar Bég O. Numerical study of transient magnetohydro-dynamic radiative free convection nanofluid flow from a stretching permeable surface. *Proc IMechE-Part E: J Proc Mech Eng* 2014; 228:181-196.
17. Takhar HS, Chamkha AJ and Nath G. Unsteady flow and heat transfer on a semi-infinite flat plate with an aligned magnetic field. *Int J Eng Sci* 1999; 37:1723-1736.
18. Gorla RSR, Ramaligham K and Adluri I. Magnetohydrodynamic braking. *ASME J Tribol* 1995;117(4):724–728.
19. Frizen VE and Sarapulov FN. Formation of MHD processes in induction crucible furnace at single-phase supply of inductor. *Russian Electrical Eng* 2010; 1(3):159-164.
20. Chen TM. Radiation effects on magnetohydrodynamic free convection flow, Technical Note. *AIAA J Thermophys Heat Transfer* 2008;22(1):125-128.
21. Kumari M and Nath G. Steady mixed convection stagnation-point flow of upper-convected Maxwell fluids with magnetic field. *Int J Non-Linear Mech* 2009; 44:1048-1055.
22. Zueco J and Anwar Bég O. Network numerical analysis of hydromagnetic squeeze film between rotating disks with magnetic Reynolds number effects. *Tribology Int* 2010;43: 532–543.
23. Anwar Bég O, Bakier AY, Prasad VR, Zueco J and Ghosh SK. Nonsimilar, laminar, steady, electrically-conducting forced convection liquid metal boundary layer flow with induced magnetic field effects. *Int J Thermal Sci* 2009;48(8):1596-1606.
24. Ahmed S, Anwar Bég O, Vedad S, Zeinalkhani M and Heidari A. Mathematical modelling of magneto-hydrodynamic transient free and forced convective flow with induced magnetic field effects. *Int J Pure Appl Sci Tech* 2012;11(1):109-125.
25. Mahmood M, Asghar S and Hossain MA. Hydromagnetic flow of viscous incompressible fluid past a wedge with permeable surface. *ZAMM: J Appl Math Mech* 2009; 89(3):174-188.
26. Haque MM, Alam MM, Ferdows M and Al-Mdallal QM. Numerical simulation and stability analysis on MHD free convective heat and mass transfer unsteady flow through a porous medium in a rotating system with induced magnetic field. *Int J Appl Electro-magnetics and Mech* 2013; 41: 121-141.
27. Ghosh SK, Anwar Bég O and Zueco J. Hydromagnetic free convection flow with induced magnetic field effects. *Meccanica* 2010;45(2):175-185.
28. Ghosh SK, Anwar Bég O and Zueco J. Hall effects on MHD flow in a rotating system with heat transfer characteristics. *Meccanica* 2009;44(6):741-765.
29. Rashidi MM, Anwar Bég O, Mehr NF and Rostami B. Second law analysis of hydromagnetic flow from a stretching rotating disk: DTM-Pade simulation of novel nuclear MHD propulsion systems. *Frontiers in Aerospace Eng* 2013;1(2):29-38.

30. Anwar Bég O, Bég TA, Rashidi MM and Asadi M. Homotopy semi-numerical modelling of nanofluid convection boundary layers from an isothermal spherical body, in a permeable regime. *Int J Micro Nano Therm Fluid Transp Phenom* 2012;3(4):237-266.
31. Anwar Bég O, Prasad VR and Vasu B. Numerical study of mixed bioconvection in porous media saturated with nanofluid containing oxytactic micro-organisms. *J Mech Med Bio* 2014;13: 1350067-1-1350067-26.
32. Remeli A, Arifin NM, Nazar R, Ismail F and Pop I. Marangoni-driven Boundary Layer Flow in a Nanofluid with Suction and Injection. *World App Sci J* 2012;17:21-26.
33. Khan WA, Hamad MAA and Ferdows M. Heat transfer analysis for Falkner–Skan boundary layer nanofluid flow past a wedge with convective boundary condition considering temperature-dependent viscosity. *Proc IMechE-Part N: J Nanoengineering and Nanosystems* 2013;227:19-27.
34. Sparrow EM and Yu HS. Local non-similarity thermal boundary layer solutions. *ASME J Heat Transfer* 1971; 93: 328-334.
35. Tiwari RK and Das MK. Heat transfer augmentation in a two-sided lid-driven differentially- heated square cavity utilizing nanofluids. *Int J Heat and Mass Transfer* 2007;50: 2002-2018.
36. Rashidi MM, Anwar Bég O, Mehr NF, Hosseini A and Gorla RSR. Homotopy simulation of axisymmetric laminar mixed convection nanofluid boundary layer flow over a vertical cylinder. *Theor Appl Mech* 2012;39(4):365–390.
37. Anwar Bég O, Gorla RSR, Prasad VR, Vasu B and Prashad RD. *Computational study of mixed thermal convection nanofluid flow in a porous medium*, 12th UK National Heat Transfer Conference, 30th August-1st September, Chemical Engineering Department, University of Leeds, UK, 2011.
38. Anwar Bég O and Tripathi D. Mathematica simulation of peristaltic pumping with double-diffusive convection in nanofluids: a bio-nano-engineering model. *Proc IMechE Part N: J Nanoengineering and Nanosystems* 2012; 225:99–114.
39. Rana P, Bhargava R and Anwar Bég O. Finite element modeling of conjugate mixed convection flow of $Al_2O_3$–water nanofluid from an inclined slender hollow cylinder. *Physica Scripta* 2013;87: 055005-1-055005-15.
40. Kao TT. Local nonsimilar solution for laminar free convection adjacent to a vertical wall. *ASME J Heat Transfer* 1976;98:321-322.
41. Loganathan P, Arasu PP, Kandasamy R. Local non-similarity solution to impact of chemical reaction on MHD mixed convection heat and mass transfer flow over porous wedge in the presence of suction / injection. *Appl Math Mech* 2010;31:1517-1526.
42. Mahmoud MAA and Megahed AM. Thermal radiation effect on mixed convection heat and mass transfer of a non-Newtonian fluid over a vertical surface embedded in a porous medium in the presence of thermal diffusion and diffusion-thermo effects. *J Appl Mech Tech Phys* 2013;54(1):90-99.
43. Mureithiand EW and Mason DP. Local Non-similarity solutions for a forced free boundary layer flow with viscous dissipation. *Math Comput Applic* 2010;15(4):558-573.
44. Munawar S, Mehmood A and Ali A. Unsteady local non-similar boundary-layer flow over a long slim cylinder. *Int J Physical Sci* 2011;6:7709-7716.
45. Anwar Bég O, Bakier AY, Prasad VR and Ghosh SK. Numerical modelling of non-similar mixed convection heat and species transfer along an inclined solar energy collector surface with cross diffusion effects. *World J Mech* 2011;4(1):185-196.
46. Chang TB, Anwar Bég O and Kahya E. Numerical study of laminar incompressible velocity and magnetic boundary layers along a flat plate with wall effects. *Int J Appl Math Mech* 2010;6(5):99-118.

47. Anwar Bég O. *Numerical Methods for Multi-Physical Magnetohydrodynamics, New Developments in Hydrodynamics Research,* Editors: Maximiano J Ibragimov and Miroslava A. Anisimov, Chapter 1, pp. 1-112, Nova Science, New York, USA, 2012.
48. Prasad VR, Gaffar SA and Anwar Bég O. Heat and mass transfer of a nanofluid from a horizontal cylinder to a micropolar fluid. *AIAA J Thermophysics Heat Transfer* 2015;29(1): 127-139.
49. Anwar Bég O, Gaffar SA, Prasad VR and Uddin MJ. Computational solutions for non-isothermal, nonlinear magneto-convection in porous media with Hall/ionslip currents and Ohmic dissipation. *Eng Sci Tech: An Int J* 2016;19:377-394.
50. Gaffar SA, Prasad VR and Anwar Bég O. Computational analysis of magnetohydro-dynamic free convection flow and heat transfer of non-Newtonian tangent hyperbolic fluid from a horizontal circular cylinder with partial slip. *Int J Appl Comput Math* 2015;1: 651-675.
51. Anwar Bég O, Uddin MJ and Khan WA. Bioconvective non-Newtonian nanofluid transport in porous media containing micro-organisms in a moving free stream. *J Mech Med Biol* 2015;15:1550071.1-1550071.20.
52. Keller HB. Numerical methods in boundary-layer theory. *Ann Rev Fluid Mech* 1978;10: 417–433.
53. Jang SP and Choi SUS. Effects of various parameters on nanofluid thermal conductivity. *ASME J Heat Transfer* 2007;129: 617-623.
54. Bianco V, Manca O, Nardini S and Vafai K. *Heat Transfer Enhancement with Nanofluids,* CRC Press, Florida, USA, 2017.
55. Das SK, Choi SU, Yu W and Pradeep T. *Nanofluids: Science and Technology*, Wiley Interscience, New York, USA, 2007.
56. Kuharat S. Simulation of natural convection in enclosure-based spacecraft solar systems, *MSc Dissertation, Aerospace Engineering, Department of Aeronautical and Mechanical Engineering, University of Salford, Manchester*, UK, 2017.
57. Sheikholeslami M and Bhatti MM. Active method for nanofluid heat transfer enhancement by means of EHD. *Int J Heat and Mass Transfer* 2017; 109:115-122.
58. Sheikholeslami M and Bhatti MM. Forced convection of nanofluid in presence of constant magnetic field considering shape effects of nanoparticles. *Int J Heat and Mass Transfer* 2017;111:1039-1049.
59. Abbas T, Bhatti MM and Ayub M. Aiding and opposing of mixed convection Casson nanofluid flow with chemical reactions through a porous Riga plate. *Proc Inst Mech Eng Part E: J Proc Mech Eng* 2017;232(5):519-527.
60. Bhatti MM and Rashidi MM. Effects of thermo-diffusion and thermal radiation on Williamson nanofluid over a porous shrinking/stretching sheet. *J Molecular Liquids* 2016; 221:567-573

## NOMENCLATURE

$Cf_x$ Skin friction coefficient

$C_p$ Specific heat at constant pressure

$f$ Dimensionless stream function

$g$ Dimensionless magnetic stream function

$G_1, G_2, G_3$ Additional unknown functions

$H$ Induced magnetic field

$H_1, H_2$ Perpendicular components of H

$h_1, h_2, h_3, h_4, h_5, h_6$ Initial guess function

$k_f$ Thermal conductivity of the fluid

$k_s$ Thermal conductivity of the solid

$k_{nf}$ Thermal conductivity of the nanofluid

$Nu_x$ Nusselt number

Pr Prandtl number

$\mathrm{Pr}_m$ Magnetic Prandtl number

$\mathrm{Re}_x$ Local Reynolds number

$T_w$ Wall temperature of the fluid

$T_\infty$ Temperature of the fluid in free stream

$U_\infty$ Free stream velocity

***Greek symbols***

$\beta$ Magnetic body force parameter

$\lambda$ Reciprocal of magnetic Prandtl number

$\eta$ Non-dimensional similarity variable

$\xi$ Non-dimensional transformed steam wise coordinate

$\theta$ Non-dimensional temperature function

$\rho_f$ Reference density of the fluid fraction

$\rho_s$ Reference density of the solid fraction

$\rho_{nf}$ Density of nanofluid

$\mu_f$ Viscosity of fluid fraction

$\mu_{nf}$ Effective viscosity of the conducting nanofluid

$\tau_w$ Shear stress at the wall

$\Delta T$ Temperature difference

***Subscripts***

$w$ Surface conditions

$\infty$ Conditions far away from the plate

# TABLES

**Table1**: Thermophysical properties of base fluids and nanoparticles

| | $\rho\,(kg/m^3)$ | $c_p$ (J/kg-K) | $k$ (W/m-K) | $\beta\,x10^{-5}(K^{-1})$ |
|---|---|---|---|---|
| Water | 997.1 | 4179 | 0.613 | 21 |
| Copper (*Cu*) | 8933 | 385 | 401 | 1.67 |
| Silver (*Ag*) | 10500 | 235 | 429 | 1.89 |
| Alumina ($Al_2O_3$) | 3970 | 765 | 40 | 0.85 |
| Titanium oxide($TiO_2$) | 4250 | 686.2 | 8.9538 | 0.9 |
| Ethylene Glycol | 1115 | 2428 | 0.253 | 0.65 |
| Kerosene | 8810 | 2010 | 0.15 | 99 |

**Table 2:** The errors computed for LNM guess values

| $h_1$ | $h_2$ | $h_3$ | $h_4$ | $h_5$ | $h_6$ |
|---|---|---|---|---|---|
| 0.000949851 | 0.001379252 | 0.001022167 | 0 | 0 | 0 |
| 0.000925271 | 0.001925341 | 0.001012947 | 4.8399E-12 | 1.01775E-11 | 6.951E-13 |
| 0.000869007 | 0.003640206 | 0.000991842 | 4.2975E-12 | 2.31775E-11 | 1.4775E-12 |
| 0.001489283 | 0.002385954 | 0.002009337 | 6.7671E-12 | 1.411E-11 | 1.6575E-12 |
| 0.001324148 | 0.002259827 | 0.002363328 | 6.0775E-12 | 1.55751E-11 | 2.6271E-12 |
| 0.001099444 | 0.003819783 | 0.002221256 | 5.1084E-12 | 8.393E-12 | 1.96E-12 |
| 0.001330523 | 0.004123436 | 0.001935197 | 2.4375E-12 | 1.45024E-11 | 1.3804E-12 |

**Table 3a:** Performance of different nanofluids with aluminum oxide-water nanofluid ($Al_2O_2$-$H_2O$) in percentage (increase (+) or decrease (-)), with $\lambda = 0.5$, $\beta = 0.1$, $\phi = 0.5$ and $Pr = 4.17$.

| | $f'$ (%) **LNM** | $f'$ (%) **KBM** | $f''$ (%) **LNM** | $f''$ (%) **KBM** | $g$ (%) **LNM** | $g$ (%) **KBM** |
|---|---|---|---|---|---|---|
| $\eta$ | 3.5 | 3.5 | 3.5 | 3.5 | 3.5 | 3.5 |
| Cu-water | 11.5420 | 11.5421 | -51.1415 | -51.1420 | 19.70224 | 19.70225 |
| Cu-EG | 10.4190 | 10.4189 | -43.3789 | -43.3792 | 16.9528 | 16.95279 |
| Cu-Ke | 13.2090 | 13.2087 | -65.5251 | -65.5254 | 24.88734 | 24.88737 |
| Ag-water | 12.8965 | 12.8963 | -62.4048 | -62.4049 | 23.7408 | 23.74081 |
| Ag-EG | 11.9703 | 11.9701 | -54.6423 | -54.6425 | 20.9058 | 20.90582 |
| Ag-Ke | 14.1815 | 14.1811 | -75.646 | -75.6462 | 29.0228 | 29.02279 |
| $Al_2O_3$-water | 1.5281 | 1.52782 | -4.1095 | -4.10931 | 2.0078 | 2.007811 |
| $Al_2O_3$-EG | 0 | 0 | 0 | 0 | 0 | 0 |
| $Al_2O_3$-Ke | 4.34128 | 4.34130 | -13.3181 | -13.3179 | 5.96657 | 5.966541 |
| $TiO_2$-water | 2.4427 | 2.44280 | -6.9254 | -6.92520 | 3.23427 | 3.234265 |
| $TiO_2$-EG | 0.90298 | 0.90293 | -2.4353 | -2.43531 | 1.169357 | 1.169356 |
| $TiO_2$-KE | 5.2789 | 5.27910 | -16.89497 | -16.8950 | 7.40973 | 7.409727 |

**Table 3b:** Performance of different nanofluids with aluminum oxide-water nanofluid ($Al_2O_2$-water) in percentage (increase (+) or decrease (-)), with $\lambda = 0.5$, $\beta = 0.1$, $\phi = 0.5$ and $Pr = 4.17$.

| | $g'$ (%) LNM | $g'$ (%) KBM | $g''$ (%) LNM | $g''$ (%) KBM | $\theta$ (%) LNM | $\theta$ (%) KBM | $\theta'$ (%) LNM | $\theta'$ (%) KBM |
|---|---|---|---|---|---|---|---|---|
| $\eta$ | 3.5 | 3.5 | 3.5 | 3.5 | 2 | 2 | 3.5 | 3.5 |
| Cu-water | 15.61037 | 15.61036 | -28.1743 | -28.1744 | -16.0036 | -16.0035 | -34.262 | -34.264 |
| Cu-EG | 13.8393 | 13.83932 | -22.6703 | -22.6705 | -20.3475 | -20.3474 | -43.454 | -43.455 |
| Cu-Ke | 18.5325 | 18.53254 | -39.6730 | -39.6731 | -39.78052 | -39.7804 | -73.8161 | -73.816 |
| Ag-water | 17.9506 | 17.95063 | -37.003 | -37.0031 | -16.095 | -16.0951 | -33.426 | -33.427 |
| Ag-EG | 16.3314 | 16.33142 | -30.8446 | -30.8445 | -18.65569 | -18.6557 | -39.2757 | -39.276 |
| Ag-Ke | 20.4933 | 20.49331 | -49.1553 | -49.1552 | -36.0311 | -36.0313 | -67.9665 | -67.967 |
| $Al_2O_3$-water | 1.8596 | 1.859601 | -1.47138 | -1.47137 | 3.9323 | 3.93231 | 10.3064 | 10.3063 |
| $Al_2O_3$-EG | 0 | 0 | 0 | 0 | 0 | 0 | 0 | 0 |
| $Al_2O_3$-Ke | 5.3763 | 5.376301 | -5.4495 | -5.44941 | -18.0155 | -18.0158 | -40.668 | -40.667 |
| $TiO_2$-water | 2.9728 | 2.972802 | -2.5613 | -2.56121 | -0.32007 | -0.32009 | -0.2785 | -0.2784 |
| $TiO_2$-EG | 1.0753 | 1.075304 | -0.8719 | -0.87193 | -1.92044 | -1.92041 | -4.7353 | -4.7352 |
| $TiO_2$-KE | 6.6034 | 6.603401 | -7.08446 | -7.08445 | -20.0731 | -20.0736 | -44.568 | -44.569 |

**Table 4:** Performance of different nanofluids with aluminum oxide-water nanofluid ($Al_2O_2$-water) in percentage (increase (+) or decrease (-)), with $\lambda = 1$, $\beta = 0.2$, $\phi = 0.5$ and $Pr = 4.17$.

| | $f'$ (%) | $f''$ (%) | $g$ (%) | $g'$ (%) | $g''$ (%) | $\theta$ (%) | $\theta'$ (%) |
|---|---|---|---|---|---|---|---|
| $\eta$ | 2.0 | 3.5 | 2.0 | 3.5 | 2 | 2 | 3.5 |
| Cu-water | -2.1426 | 9.813 | 9.94052 | -7.05766 | -35.09724 | 2.231 | 5.9322 |
| Cu-EG | -2.3375 | 8.7366 | 12.5095 | -7.334148 | -35.5140 | 2.5258 | 6.89655 |
| Cu-Ke | -1.69912 | 13.0242 | 9.5243 | -11.0032 | -34.1463 | 2.2779 | 6.3829 |
| Ag-water | -1.8259 | 12.1457 | 9.5453 | -6.5422 | -34.415 | 1.9073 | 4.6025 |
| Ag-EG | -1.9317 | 10.57046 | 9.91275 | -6.8291 | -34.805 | 2.19224 | 5.50458 |
| Ag-Ke | -1.3652 | 16.5625 | 9.084669 | -5.7322 | -33.4158 | 1.9299 | 5.21739 |
| $Al_2O_3$-water | -3.9098 | 3.7301 | 11.2689 | -9.0288 | -37.971 | 3.2996 | 8.333 |
| $Al_2O_3$-EG | -4.29222 | 3.04414 | 11.34448 | -9.2473 | -38.3093 | 3.7037 | 9.4707 |
| $Al_2O_3$-Ke | -3.4096 | 4.8287 | 11.0514 | -8.60227 | -37.289 | 3.51366 | 9.8591 |
| $TiO_2$-water | -3.7472 | 4.0883 | 11.2088 | -8.89434 | -37.784 | 3.2982 | 8.1 |
| $TiO_2$-EG | -4.0200 | 3.43214 | 11.30337 | -9.11138 | -38.0952 | 3.58974 | 9.3567 |
| $TiO_2$-KE | -3.27 | 5.40293 | 10.9735 | -8.43716 | -37.0272 | 3.43249 | 9.547738 |

## FIGURES

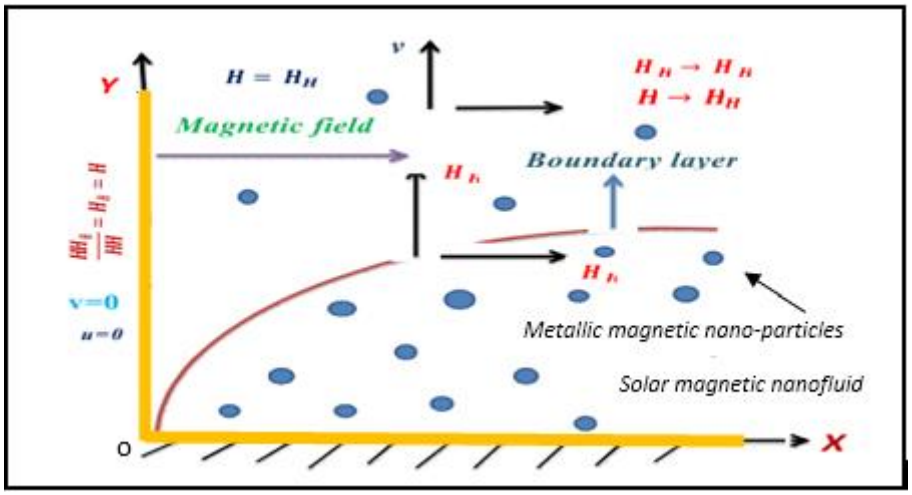


**Fig 1:** Solar magneto-nano-polymer boundary layer flow manufacturing regime

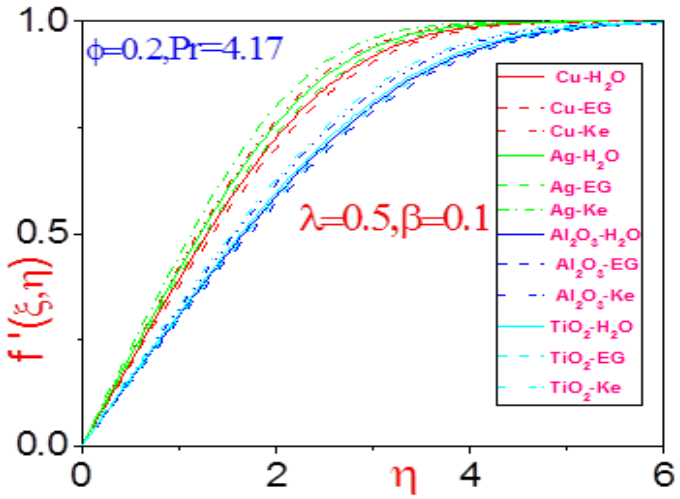


**Fig 2a:** Velocity profiles, $f'(\xi,\eta)$, for different nanofluids, with $\lambda = 0.5$, $\beta = 0.1$, $\phi = 0.2$ and $Pr = 4.17$.

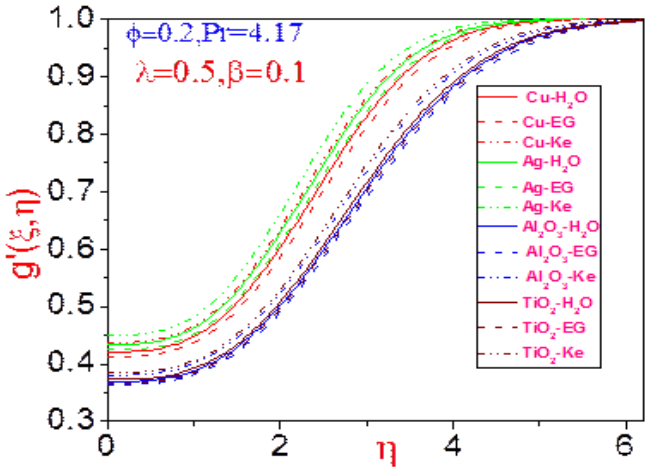


**Fig 2b:** Magnetic stream function gradient profiles, $g'(\xi,\eta)$, for different nanofluids, with $\lambda = 0.5$, $\beta = 0.1$, $\phi = 0.2$ and $Pr = 4.17$.

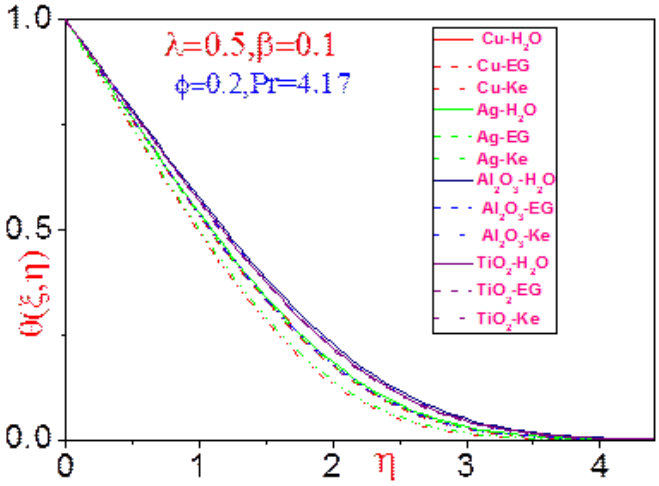


**Fig 2c:** Temperature profiles, $\theta(\xi,\eta)$, for different nanofluids, with $\lambda = 0.5$, $\beta = 0.1$, $\phi = 0.2$ and $Pr = 4.17$.

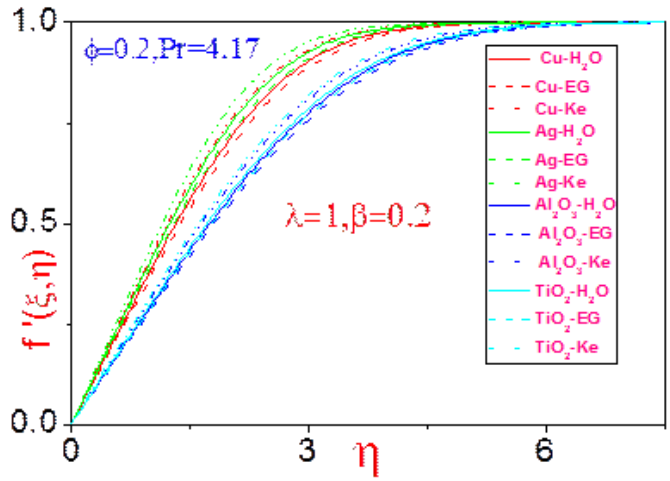


.

**Fig 3a:** Velocity distributions, $f'(\xi,\eta)$, for different nanofluids, with $\lambda = 1$, $\beta = 0.2$, $\phi = 0.2$ and $Pr = 4.17$.

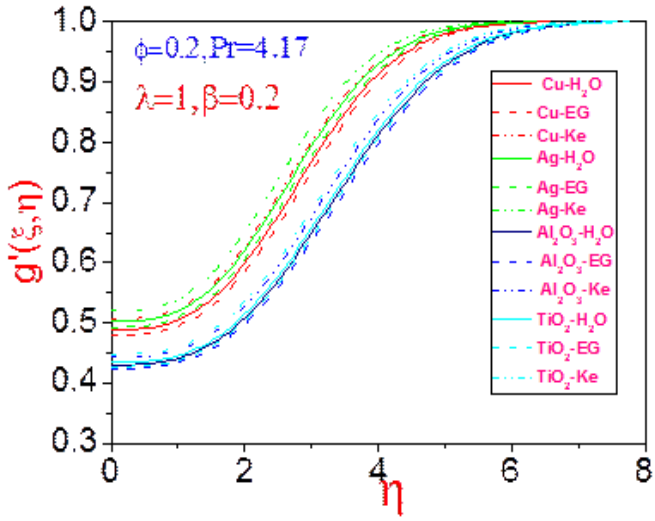


**Fig 3b:** Magnetic stream function gradient profiles, $g'(\xi,\eta)$, for different nanofluids, with $\lambda = 1$, $\beta = 0.2$, $\phi = 0.2$ and $Pr = 4.17$.

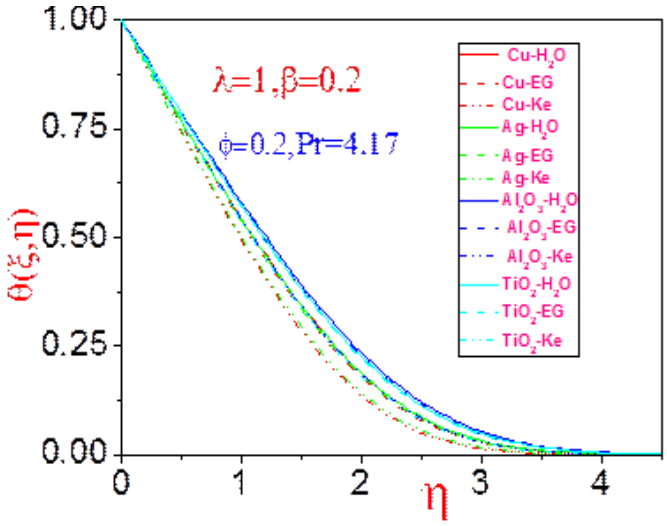


**Fig 3c:** Temperature profiles, $\theta(\xi,\eta)$, for different nanofluids, with $\lambda = 1$, $\beta = 0.2$, $\phi = 0.2$ and $Pr = 4.17$.

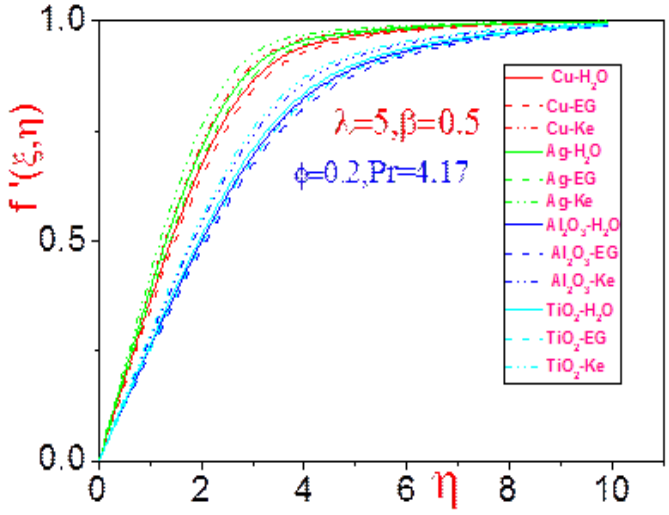


**Fig 4a:** Velocity distributions, $f'(\xi,\eta)$, for different nanofluids, with $\lambda = 5$, $\beta = 0.5$, $\phi = 0.2$ and $Pr = 4.17$.

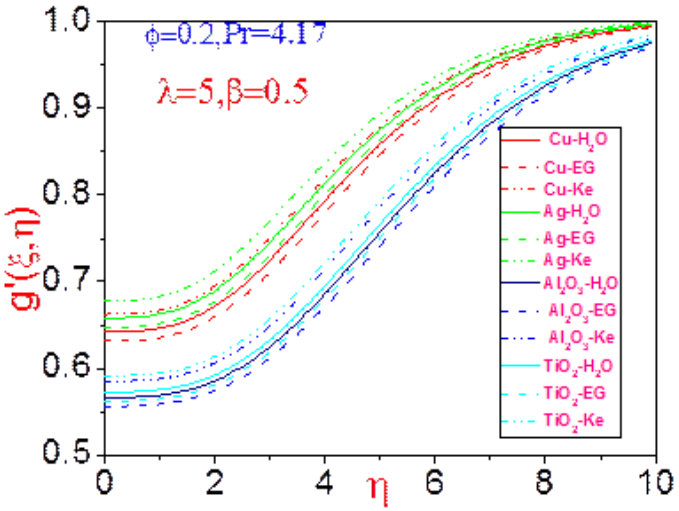


**Fig 4b:** Magnetic stream function gradient profiles, $g'(\xi,\eta)$, for different nanofluids, with $\lambda = 5$, $\beta = 0.5$, $\phi = 0.2$ and $Pr = 4.17$.

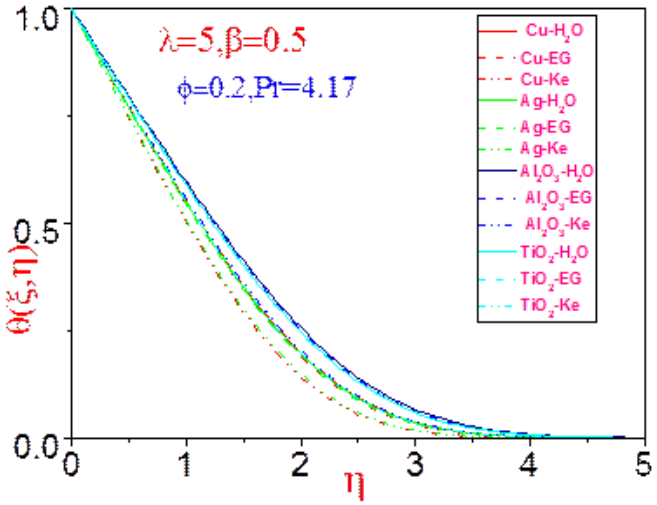


**Fig 4c:** Temperature profiles, $\theta(\xi,\eta)$, for different nanofluids, with $\lambda = 5$, $\beta = 0.5$, $\phi = 0.2$ and $Pr = 4.17$.

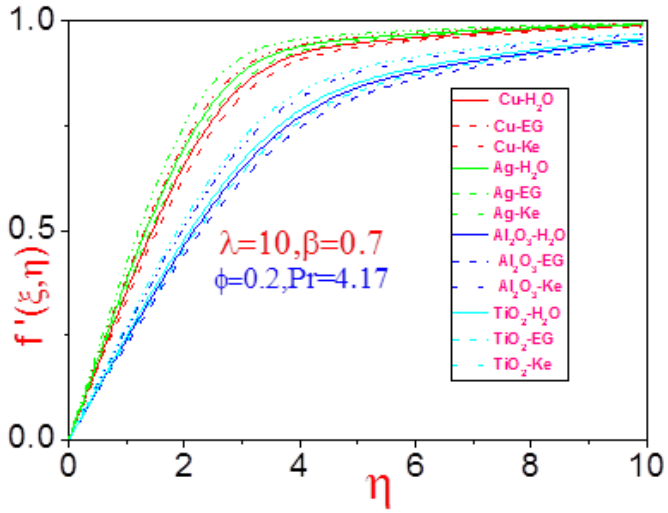


**Fig 5a:** Velocity distributions, $f'(\xi,\eta)$, for different nanofluids, with $\lambda = 10$, $\beta = 0.7$, $\phi = 0.2$ and $Pr = 4.17$.

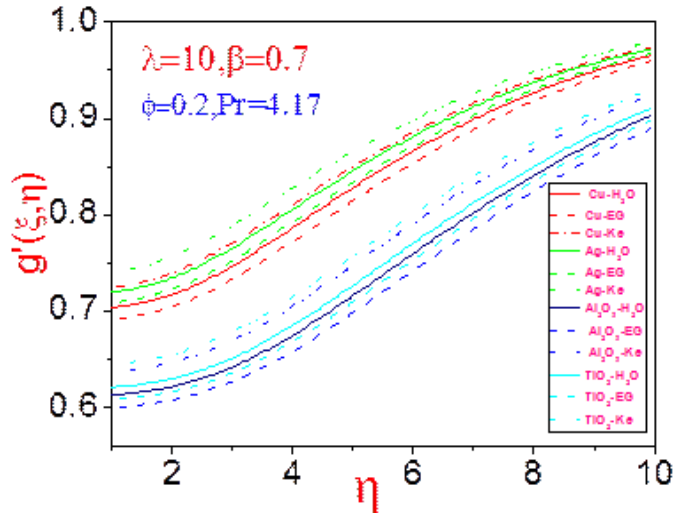


**Fig 5b:** Magnetic stream function gradient profiles, $g'(\xi,\eta)$, for different nanofluids, with $\lambda = 10$, $\beta = 0.7$, $\phi = 0.2$ and $Pr = 4.17$.

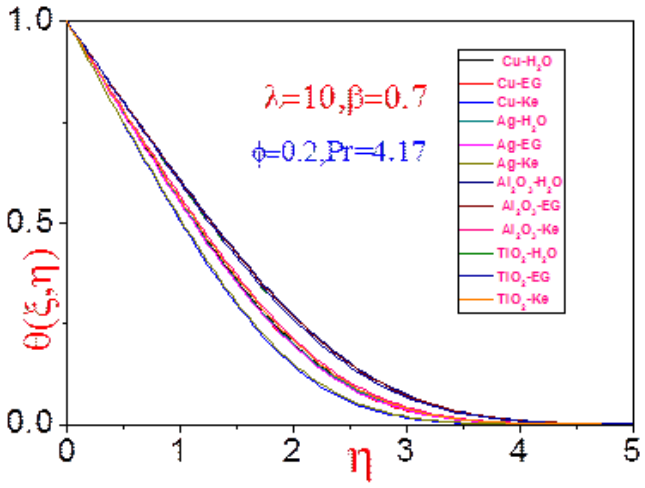


**Fig 5c:** Temperature profiles, $\theta(\xi, \eta)$, for different nanofluids, with $\lambda = 10$, $\beta = 0.7$, $\phi = 0.2$ and $Pr = 4.17$.

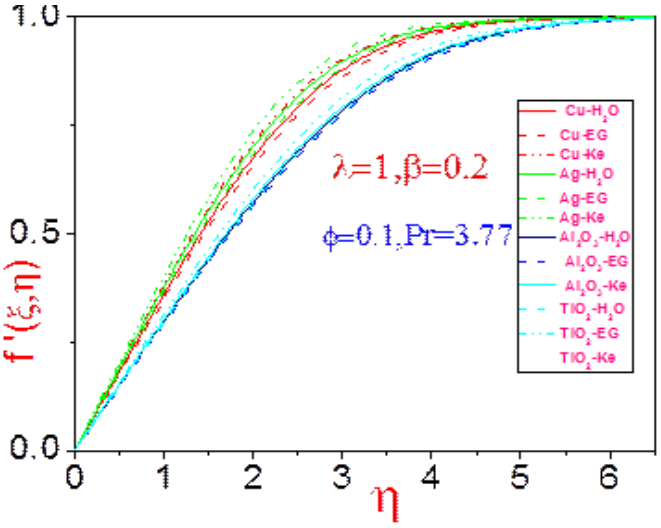


**Fig 6a:** Velocity distributions, $f'(\xi,\eta)$, for different nanofluids, with $\lambda = 1$, $\beta = 0.2$, $\phi = 0.1$ and $Pr = 3.77$.

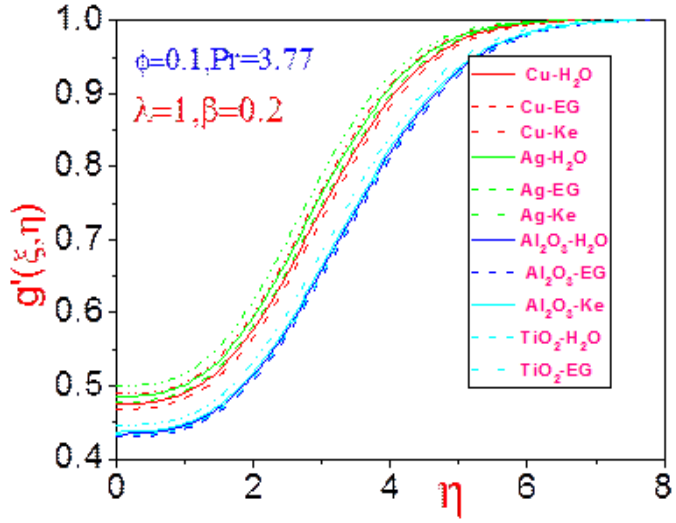


**Fig 6b:** Magnetic stream function gradient profiles, $g'(\xi,\eta)$, for different nanofluids, with $\lambda = 1$, $\beta = 0.2$, $\phi = 0.1$ and $Pr = 3.77$.

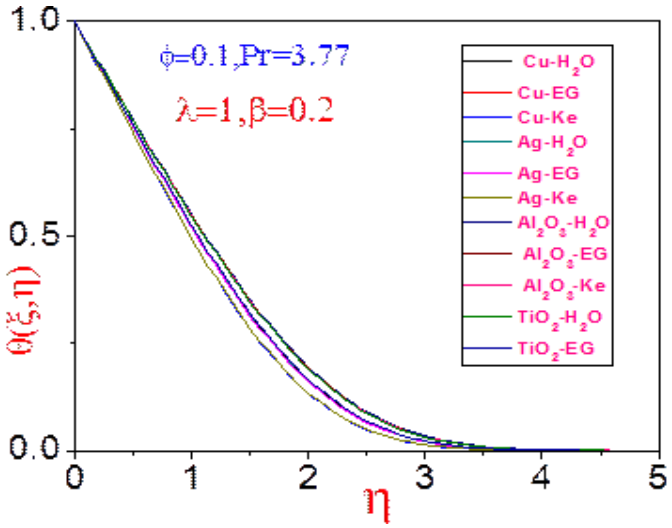


**Fig 6c:** Temperature profiles, $\theta(\xi\eta)$, for different nanofluids, with $\lambda = 1$, $\beta = 0.2$, $\phi = 0.1$ and $Pr = 3.77$.

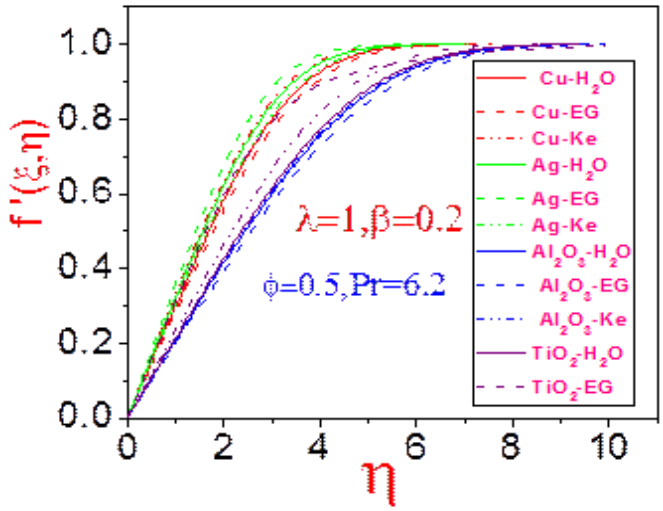


**Fig 7a:** Velocity distributions, $f'(\xi,\eta)$, for different nanofluids, with $\lambda = 1$, $\beta = 0.2$, $\phi = 0.5$ and $Pr = 6.2$.

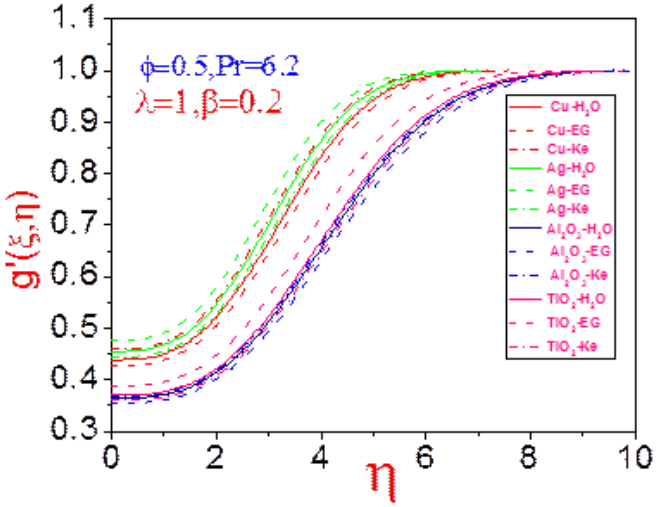


**Fig 7b:** Magnetic stream function gradient profiles, $g'(\xi,\eta)$, for different nanofluids, with $\lambda = 1$, $\beta = 0.2$, $\phi = 0.5$ and $Pr = 6.2$.

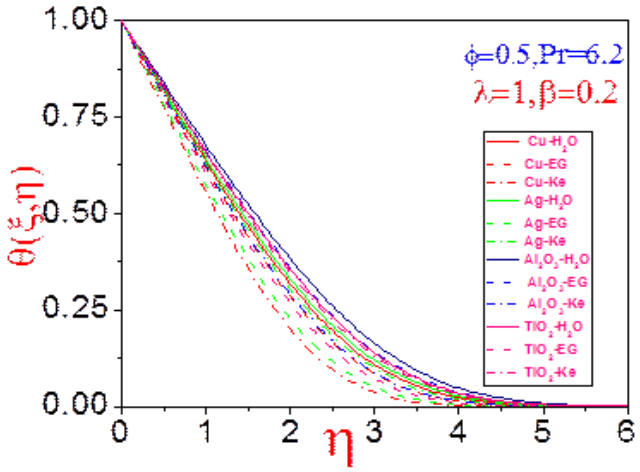


**Fig 7c:** Temperature profiles, $\theta(\xi\eta)$, for different nanofluids, with $\lambda = 1$, $\beta = 0.2$, $\phi = 0.5$ and $Pr = 6.2$.

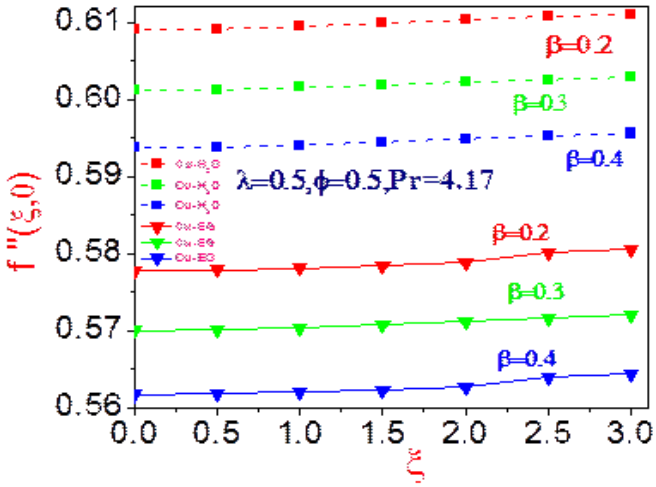


**Fig 8a:** Surface shear stress distributions, $f''(\xi,0)$ versus non-similar parameter $(\xi)$, for copper-water and copper-ethylene glycol with $\lambda = 0.5$, $\phi = 0.5$ and $Pr = 4.17$ with various magnetic body force numbers $(\beta)$.

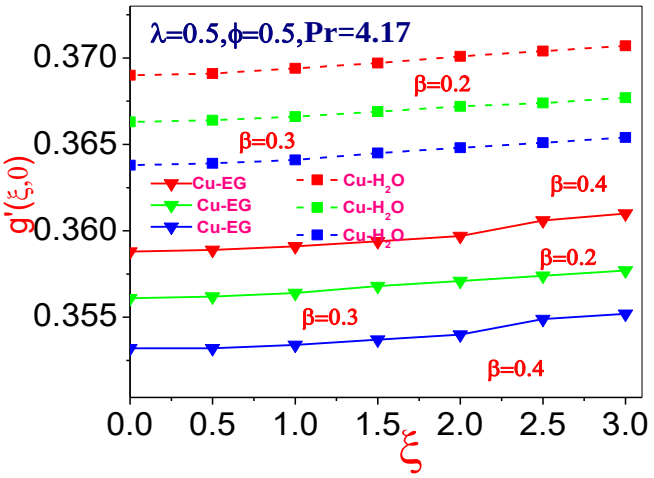


**Fig 8b:** Magnetic stream function gradient profiles, $g'(\xi,0)$, versus non-similar parameter $(\xi)$, for copper-water and copper-ethylene glycol with $\lambda = 0.5$, $\phi = 0.5$ and $Pr = 4.17$ with various magnetic body force numbers $(\beta)$.

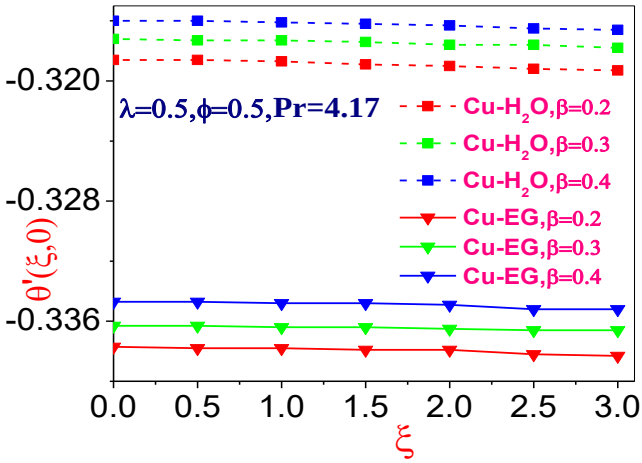


**Fig 8c:** Temperature gradient profiles, $\theta'(\xi, 0)$, versus non-similar parameter ($\xi$), for copper-water and copper-ethylene glycol with $\lambda = 0.5$, $\phi = 0.5$ and $Pr = 4.17$ with various magnetic body force numbers ($\beta$).

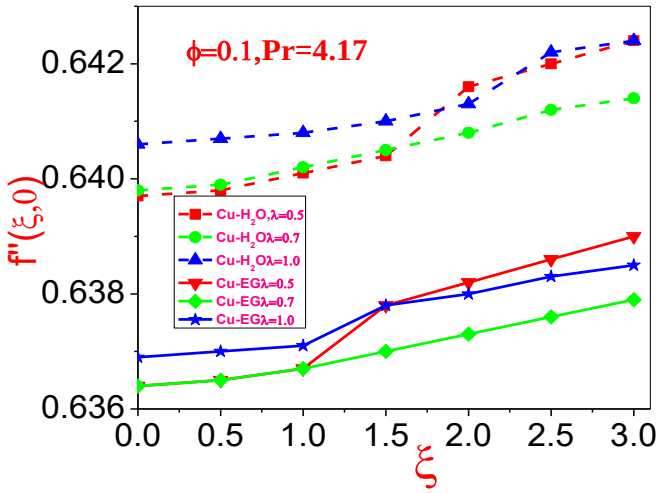


**Fig 9a:** Surface shear stress distributions, $f''(\xi,0)$ versus non-similar parameter ($\xi$), for copper-water and copper-ethylene glycol nanofluids with $\beta = 0.5$, $\phi = 0.1$ and $Pr = 4.17$ with various reciprocals of magnetic Prandtl number ($\lambda$).

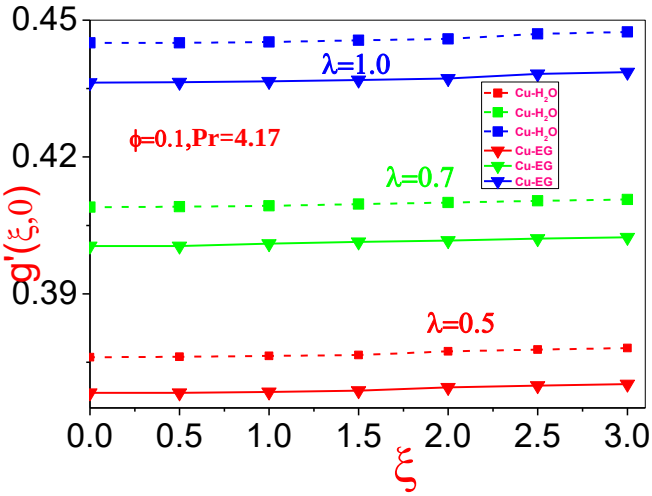


**Fig 9b:** Magnetic stream function gradient profiles, $g'(\xi,0)$, versus non-similar parameter ($\xi$), for copper-water and copper-ethylene glycol nanofluids with $\beta = 0.5$, $\phi = 0.1$ and $Pr = 4.17$ with various reciprocals of magnetic Prandtl number ($\lambda$).

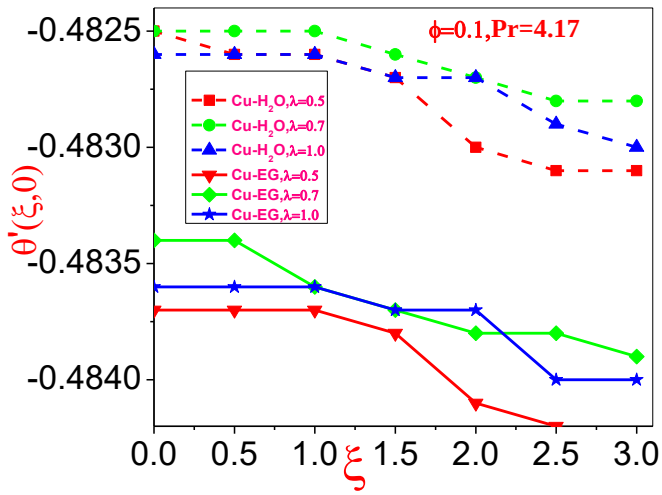


**Fig 9c:** Temperature gradient profiles, $\theta'(\xi,0)$, versus non-similar parameter ($\xi$), for copper-water and copper-ethylene glycol nanofluids with $\beta = 0.5$, $\phi = 0.1$ and $Pr = 4.17$ with various reciprocals of magnetic Prandtl number ($\lambda$).

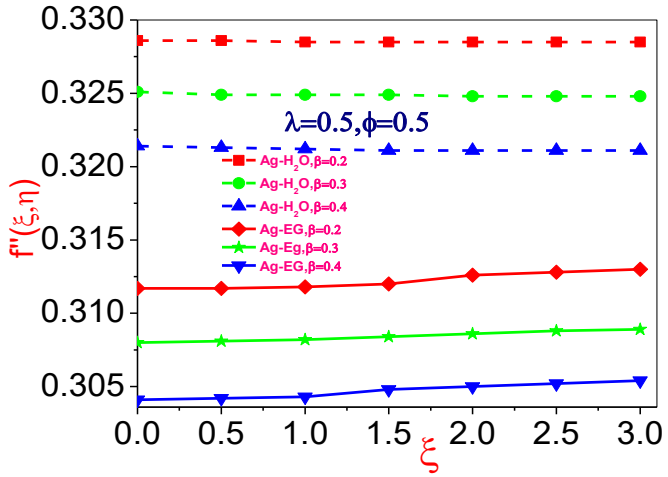


**Fig 10a:** Surface shear stress distributions, $f''(\xi,0)$ versus non-similar parameter ($\xi$), for silver-water and silver-ethylene glycol nanofluids with $\lambda = 0.5$, $\phi = 0.5$ and $Pr = 4.17$ with various magnetic body force numbers ($\beta$).

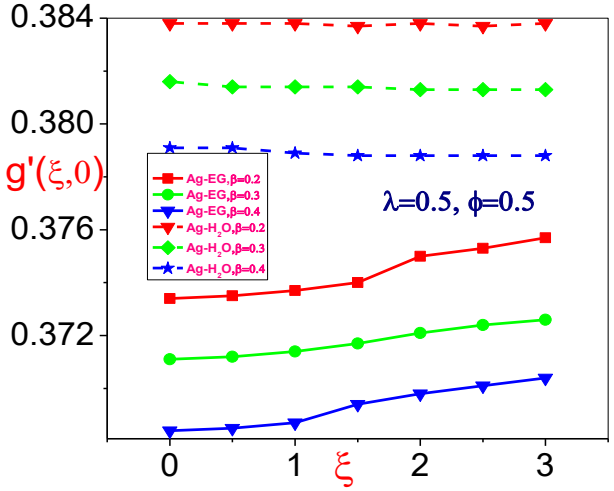


**Fig 10b:** Magnetic stream function gradient profiles, $g'(\xi,0)$, versus non-similar parameter ($\xi$), for silver-water and silver-ethylene glycol nanofluids with $\lambda = 0.5$, $\phi = 0.5$ and $Pr = 4.17$ with various magnetic body force numbers ($\beta$).

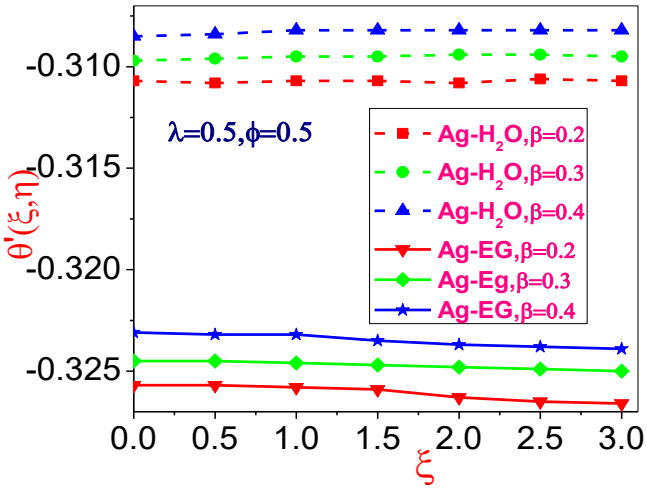


**Fig 10c:** Temperature gradient profiles, $\theta'(\xi,0)$, versus non-similar parameter ($\xi$), for silver-water and silver-ethylene glycol nanofluids with $\lambda = 0.5$, $\phi = 0.5$ and $Pr = 4.17$ with various magnetic body force numbers ($\beta$).

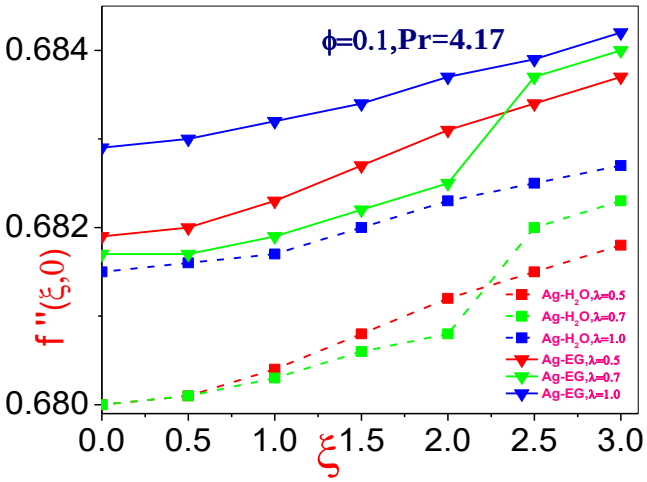


**Fig 11a:** Surface shear stress distributions, $f''(\xi,0)$ versus non-similar parameter ($\xi$), for silver-water and silver-ethylene glycol nanofluids with $\beta = 0.5$, $\phi = 0.1$ and $Pr = 4.17$ with various reciprocals of magnetic Prandtl number ($\lambda$).

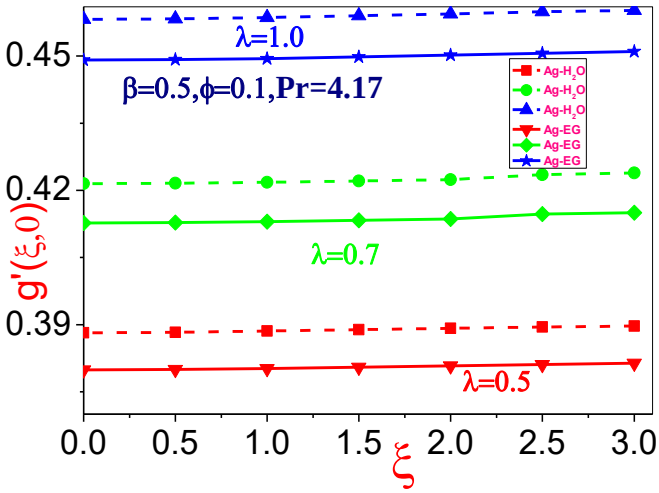


**Fig 11b:** Magnetic stream function gradient profiles, $g'(\xi,0)$, versus non-similar parameter ($\xi$), for silver-water and silver-ethylene glycol nanofluids with $\beta = 0.5$, $\phi = 0.1$ and $Pr = 4.17$ with various reciprocals of magnetic Prandtl number ($\lambda$).

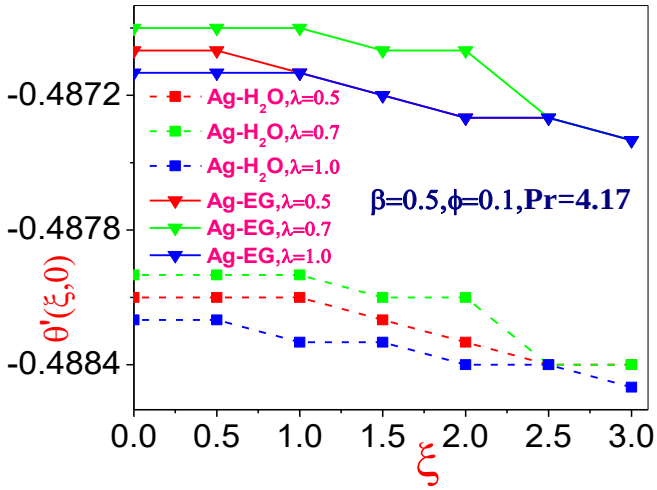


**Fig 11c:** Temperature gradient profiles, $\theta'(\xi,0)$, versus non-similar parameter ($\xi$), for silver-water and silver-ethylene glycol nanofluids with $\beta = 0.5$, $\phi = 0.1$ and $Pr = 4.17$ with various reciprocals of magnetic Prandtl number ($\lambda$).

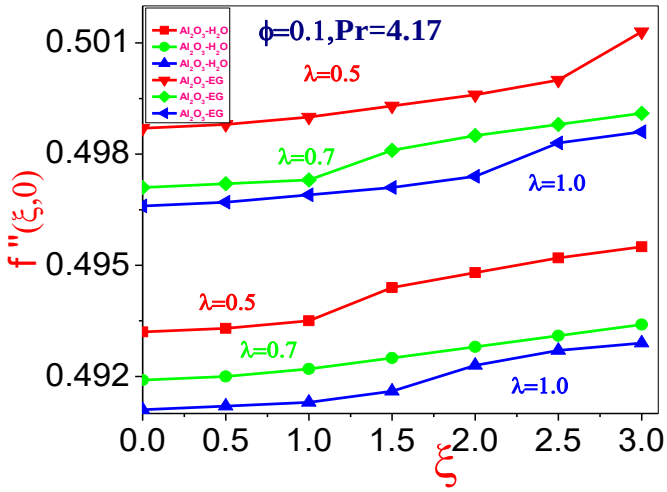


**Fig 12a:** Surface shear stress distributions, $f''(\xi,0)$ versus non-similar parameter ($\xi$), for silver-oxide water and silver oxide-ethylene glycol nanofluids with $\beta = 0.5$, $\phi = 0.1$ and $Pr = 4.17$ with various reciprocals of magnetic Prandtl number ($\lambda$).

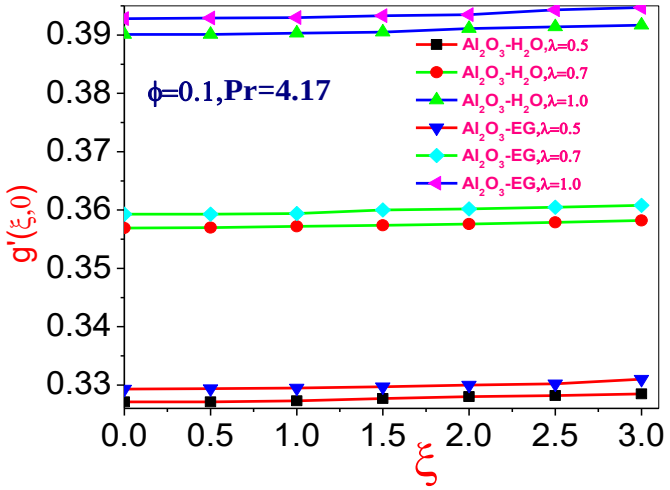


**Fig 12b:** Magnetic stream function gradient profiles, $g'(\xi,0)$, versus non-similar parameter ($\xi$), for silver-oxide water and silver oxide-ethylene glycol nanofluids with $\beta = 0.5$, $\phi = 0.1$ and $Pr = 4.17$ with various reciprocals of magnetic Prandtl number ($\lambda$).

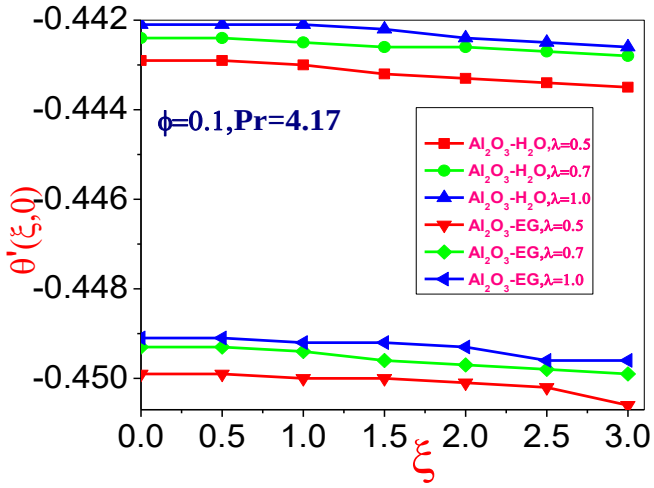


**Fig 12c:** Temperature gradient profiles, $\theta'(\xi,0)$, versus non-similar parameter ($\xi$), for silver-oxide water and silver oxide-ethylene glycol nanofluids with $\beta = 0.5$, $\phi = 0.1$ and $Pr = 4.17$ with various reciprocals of magnetic Prandtl number ($\lambda$).

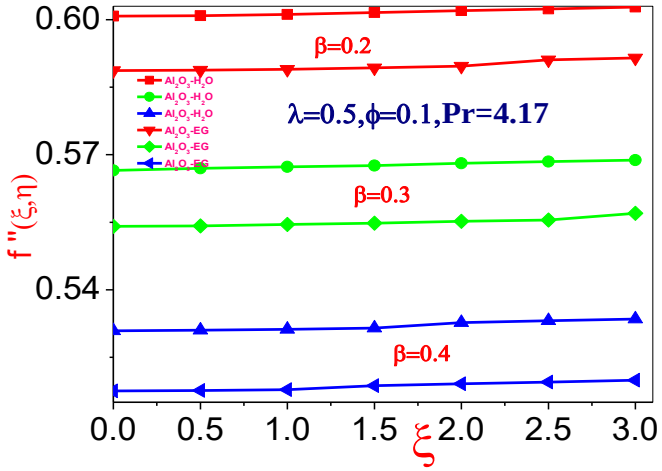


**Fig 13a:** Surface shear stress distributions, $f''(\xi,0)$ versus non-similar parameter ($\xi$), for silver-oxide water and silver oxide-ethylene glycol nanofluids with $\lambda = 0.5$, $\phi = 0.1$ and $Pr = 4.17$ with various magnetic body force numbers ($\beta$).

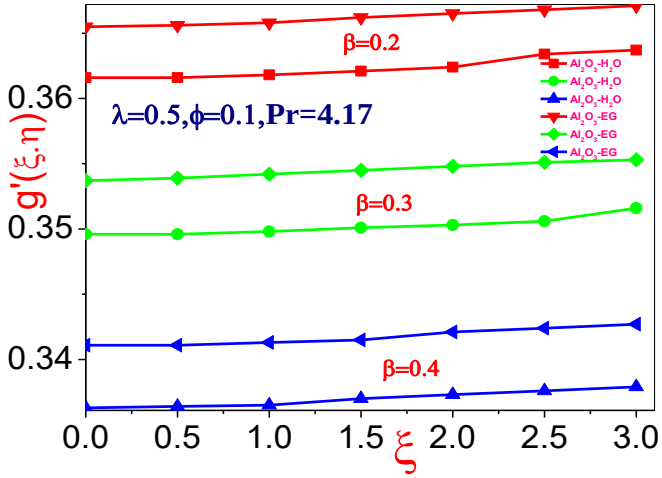


**Fig 13b:** Magnetic stream function gradient profiles, $g'(\xi,0)$, versus non-similar parameter ($\xi$), for silver-oxide water and silver oxide-ethylene glycol nanofluids with $\lambda = 0.5$, $\phi = 0.1$ and $Pr = 4.17$ with various magnetic body force numbers ($\beta$).

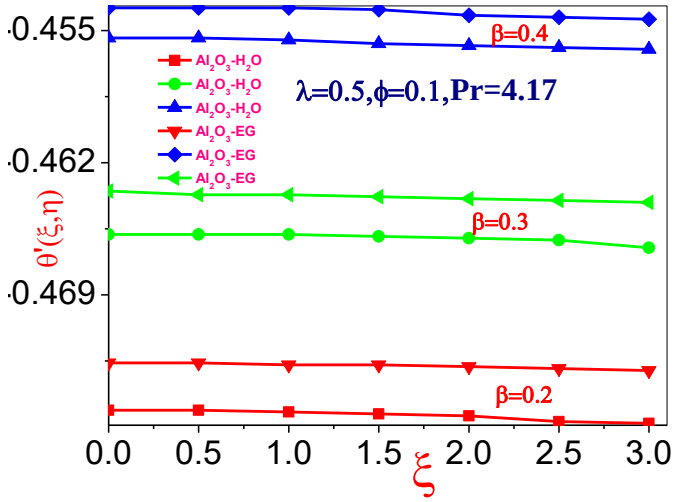


**Fig 13c:** Temperature gradient profiles, $\theta'(\xi,0)$, versus non-similar parameter ($\xi$), for silver-oxide water and silver oxide-ethylene glycol nanofluids with $\lambda = 0.5$, $\phi = 0.1$ and $Pr = 4.17$ with various magnetic body force numbers ($\beta$).